(2)

Grant AFOSR -91-0118

BASIC PROCESSES OF PLASMA PROPULSION

Herbert O. Schrade

P. Christian Sleziona

Thomas Wegmann

Helmut L. Kurtz

April 1992
Final Scientific Report

15. Nov. 1990 - 14. Nov. 1991

Approved for public release; distribution unlimited
Prepared for the
Air Force Office of Scientific Research
Bolling AFB, DC 20332-6448
through the
European Office of Aerospace Research
and Development
223/231 Old Marylebone Road
London, NW1 5th
England

(U)

SECURITY CLASSIFICATION OF THIS PAGE

REPORT DOCUMENTATION PAGE

Form Approved
OMB No. 0704-0188

1a. REPORT SECURITY CLASSIFICATION	1b. RESTRICTIVE MARKINGS
2a. SECURITY CLASSIFICATION AUTHORITY	3. DISTRIBUTION/AVAILABILITY OF REPORT Approved for public release; distribution unlimited as it appears on the report
2b. DECLASSIFICATION/DOWNGRADING SCHEDULE	
4 PERFORMING ORGANIZATION REPORT NUMBER(S)	5. MONITORING ORGANIZATION REPORT NUMBER(S)
6a. NAME OF PERFORMING ORGANIZATION Inst.f.Raumfahrtsysteme University Stuttgart 6b. OFFICE SYMBOL (If applicable) IRS	7a. NAME OF MONITORING ORGANIZATION AFOSR
6c. ADDRESS (City, State, and ZIP Code) Pfaffenwaldring 31 7000 Stuttgart 80 Germany	7b. ADDRESS (City, State, and ZIP Code) AFOSR/NA Bolling AFB DC 20332-6448
8a. NAME OF FUNDING/SPONSORING ORGANIZATION ~~EOARD / LRL~~ AFOSR London 8b. OFFICE SYMBOL (If applicable) NA	9. PROCUREMENT INSTRUMENT IDENTIFICATION NUMBER AFOSR Grant 91-0118
8c. ADDRESS (City, State, and ZIP Code) Bolling AFB DC 20332-6448 Buildg. 410	10. SOURCE OF FUNDING NUMBERS PROGRAM ELEMENT NO. 61102F PROJECT NO. 2308 TASK NO A8 WORK UNIT ACCESSION NO.

11. TITLE (Include Security Classification)

Basic Processes of Plasma Propulsion (not classified)

12 PERSONAL AUTHOR(S)

Herbert, O. Schrade; P. Christian Sleziona; Th. Rösgen; Th. Wegmann

13a. TYPE OF REPORT	13b. TIME COVERED	14. DATE OF REPORT (Year, Month, Day)	15. PAGE COUNT
	FROM 15.11.90 TO 14.11.91	April 92	42

16. SUPPLEMENTARY NOTATION

17 COSATI CODES			18. SUBJECT TERMS (Continue on reverse if necessary and identify by block number)
FIELD	GROUP	SUB-GROUP	

19 ABSTRACT (Continue on reverse if necessary and identify by block number)

The report resumes the theoretical and analytical works, which accompanies the experimental development work on plasma thrusters done at the Institute of Space Systems, University of Stuttgart.

20 DISTRIBUTION/AVAILABILITY OF ABSTRACT ☐ UNCLASSIFIED/UNLIMITED ☐ SAME AS RPT ☒ DTIC USERS	21 ABSTRACT SECURITY CLASSIFICATION (U)
22a NAME OF RESPONSIBLE INDIVIDUAL Dr. Mitat A. Birkan	22b TELEPHONE (Include Area Code) (202) 767-4938 22c. OFFICE SYMBOL NA

DD Form 1473, JUN 86 Previous editions are obsolete.

SECURITY CLASSIFICATION OF THIS PAGE

(U)

Contents

Preface

The work described in this final report has been sponsored by the Air Force Office of Scientific Research through the European Office of Aerospace Research and Development in London under Grant AFOSR-91-0118. The research work period covered herein lasted from 15. Nov 1990 to 14. Nov 1991 and presents the final one after several successive sponsoring periods. The Institut für Raumfahrtsysteme (Space Systems) of the University Stuttgart is therefore indepted and would like to thank for the longyears support on the investigation of Basic Processes of Plasma Propulsion. We also hope to have contributed helped in understanding more profoundly the fundamental processes in and assessing more deeply the performance limits of coaxial magneto plasmadynamic arc thrusters.

Nomenclature

a	factor	A	cross section
$\vec{B}$	magnetic induction	e	electronic charge
e_s	specific energy	$\vec{E}$	electric field strength
$\vec{F}$	spatial derivatives	$\vec{G}$	spatial derivatives
h	Planck's constant	$\vec{H}$	source vector
I	electric current	$\vec{j}$	current density
J	Jacobian	k	Boltzmann constant
m	mass	$\dot{m}$	mass flow rate
$m_{e\nu}$	reduced mass	$m_{i\nu}$	reduced mass
n	particle density	$\vec{n}$	normal vector
p	pressure	$\overleftrightarrow{P}$	pressure tensor
$\vec{q}$	flow variables	$\vec{q}_s$	heat flux
Q	cross section	r	radial coordinate
R	radius	$\vec{t}$	tangential vector
$\vec{T}$	thrust	t	time
T	temperature	u	velocity
U	contravariant velocity	v	velocity
V	contravariant velocity	V_c	volume
z	axial coordinate	z_i	charge number
α	heat transfer coefficient	β	plasma parameter
ϵ_{ion}	ionisation energy	η	curvilinear coordinate
λ	thermal conductivity	μ	viscosity coefficient
μ_0	permeability in vacuum	ξ	curvilinear coordinate
ϱ	mass density	σ	electric conductivity
τ	electron collision time	Ψ	stream function
ω	electron gyrofrequency		

Subscripts

e	electron	h	heavy particles
i	ions	r	radial
rct	reaction	s	surface
z	axial	ν	paricles
θ	azimuthal		

1 Introduction

Since more than one decade the Institute of Space Systems, University of Stuttgart is engaged in developing, testing and assessing the performance of various types of steady state coaxial plasmathrusters. These thrusters [1, 2, 3] consist of a cathode rod in the center and a cylindrical and/or nozzle shaped discharge chamber which serves in the whole or in part as an anode. The gaseous propellant enters the arc discharge becomes Joule– heated and ionized and assumes the lokal speed of sound somewhere in the nozzle throut or of the constant cross sectional area of the thruster; the plasma is than further accelerated eigther by termal expansion through a bell shaped nozzle and/or by axial electromagnetic forces. Depending on whether the first or the second acceleration mechanisme is predominant, one speaks of an arc jet or an magnetoplasmadynamic (MPD) thruster device. So far only self magnetic thrusters have been investigated and developed at the Institut of Space Systems.

This experimental work is accompanied by theoretical investigations[4, 5, 6] in order to get a more profound knowledge of the plasma behavior and the critical conditions which limit the performance and applicability of these thrusters. Therefore in this report the computational methode and the more reasant code development will be addressed first. Afterwards a profound analysis and a new explanation of the well known performance limiting onset phenomenon is presented. Excellent agreement is found between calculated and measured onset conditions for the various thruster types which proves the validity of this new explanation.

2 Code Development

Despite of the simplicity in design of a coaxial plasma thruster (see Fig. 1) the physics of those thrusters is extremly complex and by no means fully understood. For instance the cathode– and anode attachment of the arc or the arc boundary given by the free stream transitions layer between the electrically conducting plasma and the not conduction colder gasstream should be known better. But despite of these problems various codes have been developed so far to calculate the thruster performance based on one-dimensional [1, 7] , quasi two-dimensional [4, 8] and simplified two-dimensional codes assuming proper boundary conditions.

In this report, a new two-dimensional axisymmetric code is presented, for an MPD thruster with argon as propellant allowing ionization up to the sixth level. The extended Ohm's law is used to calculate the current contour lines; the electron temperature distribution was solved by including the electron energy equation, whereas a two-dimensional flow code is used to obtain the velocity, pressure and heavy particle temperature distributions. With this formulation the thermal nonequilibrium in the plasma flow is taken into account. However, the composition of the plasma is calculated by means of the electron temperature dependent Saha equation for the different ionization levels, the conservation of mass and the electrical charge neutrality.

A comparison of the numerical and experimental results for different currents will be presented and discussed in this report.

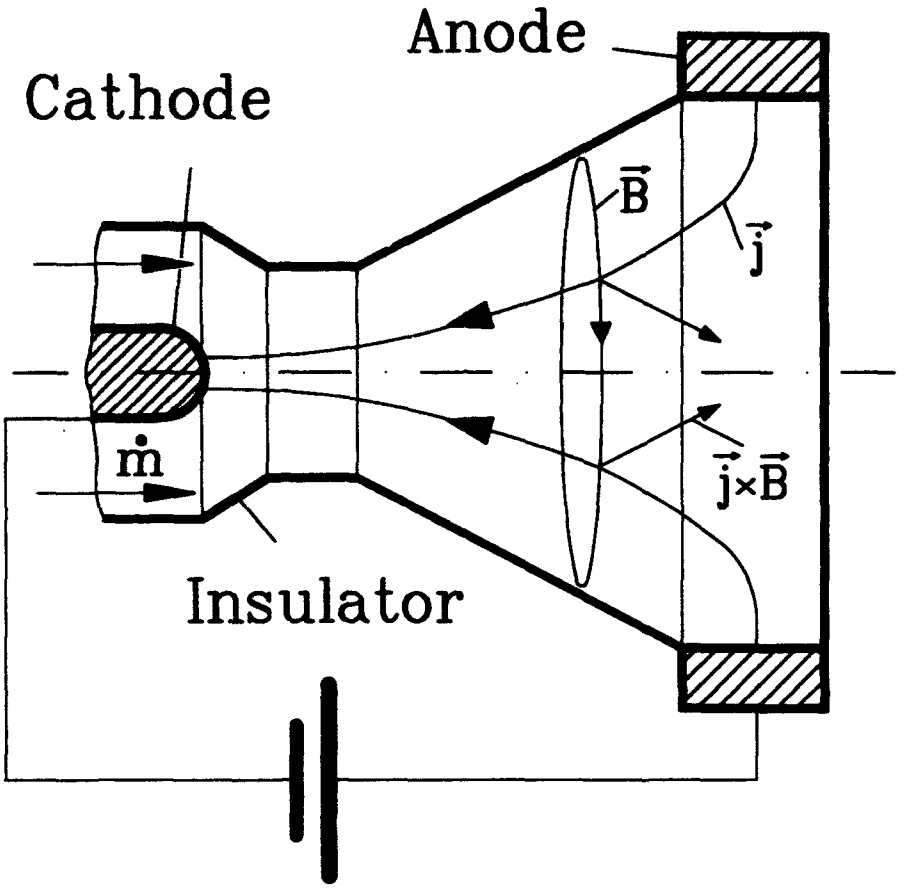

Figure 1: Principle Scheme of a Coaxial Plasmathruster.

2.1 Outline of the Computational Method

The physical and numerical modeling of this problem was developed at the IRS [4, 7] For the calculation of the MPD flow, a program system is applied which connect three different physical fields to one another. The three program system parts are the extended Ohm's law for plasma to calculate the discharge, the electron energy equation to calculate the electron temperature and the flow code to obtain the properties of the flow field. The flow calculation was done first by a one-dimensional flow code which is still applied here for the simulations of plasma thrusters called nozzle type MPD accelerators. However, a fully two-dimensional Euler code is used in this report for a cylindrical configuration of an MPD accelerator, with conical cathode.

The three codes are connected in the following manner: for a given flow field and an electron temperature distribution, the current, and hence the magnetic field distribution, was determined. With the ohmic heating, as a result of the current distribution, an electron energy calculation follows and determines a new electron temperature distribution. With these results the flow field equations were integrated. In the next time step, this new flow field and the new electron temperature distribution were taken to calculate the new electromagnetic field distribution, and so on. In the following paragraphes the basic equations of the three systems are presented.

2.2 Discharge Code

The current distribution within a selffield MPD thruster is assumed to be two-dimensional no azimuthal current has to be expected. In order to calculate the current distribution of such an arc discharge, a two-dimensional computer code has been developed. The basic equation for the discharge is the extended Ohm's law for plasmas:

$$\vec{j} = \sigma(\vec{E} + \vec{v} \times \vec{B}) - \frac{\omega_e \tau_e}{B}(\vec{j} \times \vec{B}) - \beta \nabla p_e \tag{1}$$

Here is σ the electric conductivity, ω_e the electron cyclotronfrequency and τ_e the electron collision time. Rewriting the Ohm's law by means of Maxwell's equations, one obtains a vector equation for the magnetic induction vector $\vec{B}$ in the form

$$0 = \frac{1}{\mu_0}(\nabla \times (\frac{1}{\sigma}\nabla \times \vec{B})) - (\nabla \times (\vec{v} \times \vec{B})) + \frac{1}{\mu_0}(\nabla \times (\beta(\nabla \times \vec{B}) \times \vec{B})) - \nabla\beta\nabla p_e \tag{2}$$

with

$$\beta = \frac{\omega\tau}{B_\theta \sigma} = \frac{1}{en_e} \tag{3}$$

With the Jacobian J of the transformation from cylindrical to the curvilinear coordinates:

$$J = \frac{1}{\frac{\partial z}{\partial \xi}\frac{\partial r}{\partial \eta} - \frac{\partial z}{\partial \eta}\frac{\partial r}{\partial \xi}} \tag{4}$$

the matrices are formed in terms of the derivatives of the cylindrical coordinates as follows:

$$\begin{aligned} \xi_z &= J\frac{\partial r}{\partial \eta}, \qquad \eta_z = -J\frac{\partial r}{\partial \xi} \\ \xi_r &= -J\frac{\partial z}{\partial \eta}, \qquad \eta_r = J\frac{\partial z}{\partial \xi} \end{aligned} \tag{5}$$

where the convention $\xi_z = \frac{\partial \xi}{\partial z}$, etc. is used.

The equation (2) yields with a stream function $\Psi = r\,B_\theta$ the elliptical, partial differential equation of 2nd order

$$\begin{aligned} &\frac{\partial^2\Psi}{\partial\xi^2}\left(\xi_z^2 + \xi_r^2\right) + 2\frac{\partial^2\Psi}{\partial\xi\partial\eta}\left(\xi_z\eta_z + \xi_r\eta_r\right) + \frac{\partial^2\Psi}{\partial\eta^2}\left(\eta_z^2 + \eta_r^2\right) \\ &+ \frac{\partial\Psi}{\partial\xi}\left\{\xi_z\frac{\partial\xi_z}{\partial\xi} + \eta_z\frac{\partial\xi_z}{\partial\eta} + \xi_r\frac{\partial\xi_r}{\partial\xi} + \eta_r\frac{\partial\xi_r}{\partial\eta}\right. \\ &+ \xi_z\left[-\frac{1}{\sigma}\left(\xi_z\frac{\partial\sigma}{\partial\xi} + \eta_z\frac{\partial\sigma}{\partial\eta}\right) - \left(\frac{\sigma\Psi}{r} - \frac{\partial p_e}{\partial\xi}\right)\left(\xi_r\frac{\partial\beta}{\partial\xi} + \eta_r\frac{\partial\beta}{\partial\eta}\right) + \frac{2\sigma\beta\Psi}{r^2} - \sigma\mu_0 u\right] \\ &+ \left.\xi_r\left[-\frac{1}{r} - \frac{1}{\sigma}\left(\xi_r\frac{\partial\sigma}{\partial\xi} + \eta_r\frac{\partial\sigma}{\partial\eta}\right) + \left(\frac{\sigma\Psi}{r} - \frac{\partial p_e}{\partial\eta}\right)\left(\xi_z\frac{\partial\beta}{\partial\xi} + \eta_z\frac{\partial\beta}{\partial\eta}\right) - \sigma\mu_0 v\right]\right\} \\ &+ \frac{\partial\Psi}{\partial\eta}\left\{\xi_z\frac{\partial\eta_z}{\partial\xi} + \eta_z\frac{\partial\eta_z}{\partial\eta} + \xi_r\frac{\partial\eta_r}{\partial\xi} + \eta_r\frac{\partial\eta_r}{\partial\eta}\right. \\ &+ \eta_z\left[-\frac{1}{\sigma}\left(\xi_z\frac{\partial\sigma}{\partial\xi} + \eta_z\frac{\partial\sigma}{\partial\eta}\right) - \left(\frac{\sigma\Psi}{r} - \frac{\partial p_e}{\partial\eta}\right)\left(\xi_r\frac{\partial\beta}{\partial\xi} + \eta_r\frac{\partial\beta}{\partial\eta}\right) + \frac{2\sigma\beta\Psi}{r^2} - \sigma\mu_0 u\right] \\ &+ \left.\eta_r\left[-\frac{1}{r} - \frac{1}{\sigma}\left(\xi_r\frac{\partial\sigma}{\partial\xi} + \eta_r\frac{\partial\sigma}{\partial\eta}\right) + \left(\frac{\sigma\Psi}{r} - \frac{\partial p_e}{\partial\xi}\right)\left(\xi_z\frac{\partial\beta}{\partial\xi} + \eta_z\frac{\partial\beta}{\partial\eta}\right) - \sigma\mu_0 v\right]\right\} \\ &+\sigma\mu_0\Psi\left(\frac{v}{r} - \frac{\partial U}{\partial\xi} - \frac{\partial V}{\partial\eta}\right) = 0 \end{aligned} \tag{6}$$

with U and V as the contravariant velocities

$$\begin{aligned} U &= \xi_z u + \xi_r v \\ V &= \eta_z u + \eta_r v \end{aligned} \tag{7}$$

The function $\Psi(r,z) = const$ now represents a current contour line, since $B = B_\theta$ is proportional to $\frac{I(r)}{R}$, where $I(r)$ is the electric current carried through the cross sectional area πr^2. The proper boundary conditions for Ψ follow from the geometry of the thruster walls and electrodes. At the insulator inside the thruster and at the inflow boundary Ψ is set to $-\frac{\mu_0}{2\pi} I$. For the electrodes the electric field is assumed to be normal to the surfaces $\vec{E} \cdot \vec{t} = 0$. In accordance with the curvilinear grid, where the η coordinates are perpendicular to the electrodes, it is equal to $E_\xi = 0$, and it follows to:

$$\frac{\partial \Psi}{\partial \eta} \left[\frac{\beta \Psi}{R} (\xi_r \eta_r - \xi_z \eta_z) + \frac{1}{\sigma} (\xi_z \eta_r - \xi_r \eta_z) \right] + \frac{\partial \Psi}{\partial \xi} \frac{\beta \Psi}{R} \left(\xi_r^2 - \xi_z^2 \right) + \mu_0 \Psi (\xi_r u - \xi_z v) = 0 \tag{8}$$

At the other boundary sections and at the symmetry axis Ψ is set to 0. The composition of the Argon Plasma is calculated as following.

Due to the higher mobility of the electrons, the ionization of the argon plasma in MPD thrusters is dominated by the electron temperature. The Saha equations for the different ionization levels [8, 20], (i=1,2,...,6) follow by

$$\frac{n_{i+1}}{n_i} p_e = \frac{g_{i+1}}{g_i} 2 \frac{(2\pi m_e)^{3/2} (kT_e)^{5/2}}{h^3} e^{-\frac{\epsilon_i}{kT_e}} \tag{9}$$

Here p_e is the partial pressure of the electrons, n_i the number densities, g_i the weighting factor taking into account the degenerated states and ϵ_i the ionization energy of the ionization level i.

The sum of the partial pressures of all plasma components yields the total pressure

$$p = \sum_\nu n_\nu \, k \, T_\nu \tag{10}$$

and the neutrality of charge

$$n_e = \sum_i z_i \, n_i \tag{11}$$

considering the higher ionization modes up to the sixth ionization level the eqations 9 – 11 yield a seventh order polynom for the electron density. In equation 10 represents T_ν the electron temperature T_e and the heavy particles temperature, which for all heavy particles is equal T_h. In eqation 11 z_i stands for the charge number.

The eqation for the electron density is solved by a Newton iteration. With this electron density the other partial densities like the argon atoms and the different ions are determined.

The electric conductivity of an plasma is determined by[9, 21]:

$$\sigma = \frac{3}{8} \sqrt{\frac{\pi}{2}} \frac{e^2 n_e}{\sum_{\nu(\neq e)} n_\nu Q_{e\nu} \sqrt{m_{e\nu} k T_{e\nu}}} \tag{12}$$

Here $m_{e\nu}$ is the reduced mass and $T_{e\nu}$ the reduced temperature. With respect to the different ionized levels the Gvosdover cross sections follows by[10, 11, 23]:

$$Q_{ei} = \frac{\pi}{4} \left(\frac{z_i e^2}{4\pi\epsilon_o k T_e} \right)^2 ln \left(144\pi^2 \frac{\epsilon_o^3 T_e^3 k}{n_e e^6 (z_i^2 (z_i + 1))} \right)$$

For $Q_{e\nu}$ being the cross section between electrons and atoms in equation 12 the Ramsauer cross section is used [12, 24]. From these eqations it is obviously that the high ionization levels have a strong effect on the electric conductivity.

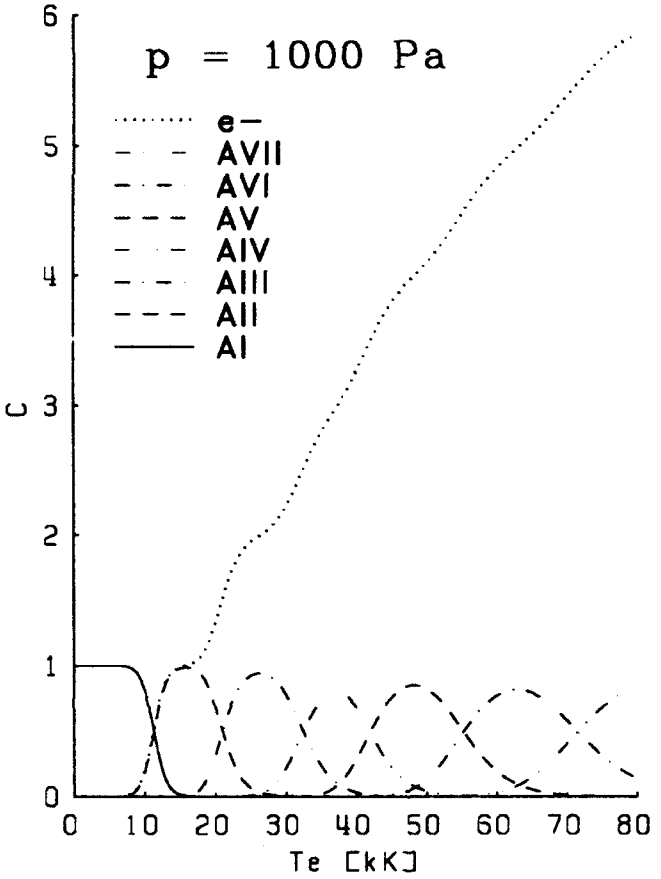

Figure 2: Composition of an argon plasma as function of electrontemperature at 1000 Pa.

For an electron temperature up to $80\,kK$ and a constant pressure of $1000\,Pa$ in Fig. 2, a typical concentration distribution with respect to the sum of heavy particles is presented. With the model developed here for higher ionisation levels it is obvious that calculations for typical MPD conditions are possible up to an electron temperature of nearly $80\,kK$.

2.3 Electron Energy Equation

The electron temperature has a strong effect on the electrical and thermal conductivity and on the electron density, which again influences the discharge pattern. Therefore, a two-dimensional code for the electron temperature distribution, corresponding to the two-dimensional discharge code, was written. The electron temperature distribution is determined by the energy equation for the electron component of the plasma.

$$\nabla(\lambda_e \nabla T_e) + \frac{5}{2}\frac{k}{e}\vec{j}\nabla T_e + p_e \nabla \cdot \vec{v} = \frac{\vec{j}^2}{\sigma} - \sum_{\nu} n_\nu n_e \alpha_{e\nu}\,(T_e - T_h) - \epsilon_i \left.\frac{\partial n_e}{\partial t}\right|_{rct} \qquad (13)$$

The subscript ν represents the heavy particles. The first term on the left hand side represents the heat flux in the electron gas, and the second term gives the convective change of the electron gas energy due to the electron drift. The energy input due to ohmic heating is represented by the first term on the right hand side. The sum of losses due to the energy transfer from the electron gas to the heavy particles gas is calculated by the second term on the right hand side. The reaction losses are given by the last term, where ϵ_i is given by Unsöld [8, 20]. The heat transfer coefficient $\alpha_{e\nu}$ and the thermal conductivity λ_e depend on the electron temperature and follow from kinetic theory[21, 22, 26]

$$\alpha_{e\nu} = \frac{8\sqrt{2}}{\sqrt{\pi}} Q_{e\nu} \sqrt{\mu_{e\nu} k T_{e\nu}} \frac{k}{m_e + m_\nu} \tag{14}$$

and the thermal conductivity:

$$\lambda_e = \frac{15}{8}\sqrt{\frac{\pi}{2}} \frac{n_e k^2 T_e \left(1 + \frac{1}{2}\frac{T_e}{n_e}\frac{\partial n_e}{\partial T_e}\right)}{\sum_{\nu(=e)} n_\nu Q_{e\nu} \frac{m_e}{m_e + m_\nu} \sqrt{m_\nu k T_\nu}} \tag{15}$$

In the sum of this conductivity equation includes ν also the electron component. For $\nu = e$ the colission cross section Q_{ee} can be set equal to the Gvosdover cross section[10, 23]. If $Q_{e\nu}$ being the cross section between the electrons and ions, the Gvosdover cross section is used with respect to the different ionization levels, and for $Q_{e\nu}$ being the cross section between electrons and atoms the Ramsauer cross section is used [12, 24].

With respect to the rotational symmetry, equation 13 results in the following elliptical, partial differential equation of 2nd order:

$$\begin{aligned}
&(\eta_r^2 + \eta_z^2)\frac{\partial^2 T_e}{\partial \xi^2} + (\xi_z^2 + \xi_r^2)\frac{\partial^2 T_e}{\partial \eta^2} + 2(\xi_z\eta_z + \xi_r\eta_r)\frac{\partial^2 T_e}{\partial \xi \partial \eta} + \\
&\frac{J^2}{4\lambda_{ec} T_e^{5/2}}\left[\sum_\nu n_e n_\nu \alpha_{e\nu}(T_h - T_e) + \frac{\vec{j}^2}{\sigma} - \epsilon_i\left(u\frac{\partial n_{e,rct}}{\partial \xi} + v\frac{\partial n_{e,rct}}{\partial \eta}\right) - \right. \\
&\frac{3 n_e k}{2J}\left(u r_\eta \frac{\partial T_e}{\partial \xi} - u r_\xi \frac{\partial T_e}{\partial \eta} + v z_\xi \frac{\partial T_e}{\partial \eta} - v z_\eta \frac{\partial T_e}{\partial \xi}\right) - \\
&\left.\frac{n_e k T_e}{J}(r_\eta u_\xi - r_\xi u_\eta + z_\xi v_\eta - z_\eta v_\xi)\right] - a_1\frac{\partial T_e}{\partial \eta} - a_2\frac{\partial T_e}{\partial \xi} = 0
\end{aligned} \tag{16}$$

Here ξ and η indicate the partial differentiation to the curvilinear $\xi-$ and $\eta-$ directions. J is the Jacobian of the transformation and a_1 , a_2 are metric terms.

At the outflow boundary T_e is set to a value in accordance with measurements[13, 25]. The solid bodies of the thruster are treated as thermal insulators. Therefore the boudary condition inside the thruster is given by $\nabla T_e \cdot \vec{n} = 0$, where $\vec{n}$ is the normal vector of the surfaces. Due to the axial symmetry, $\frac{\partial T_e}{\partial r} = 0$ on the axis. At the inflow boundary T_e is set to a constant value of $7000\,K$ in accordance with the measurements.

2.4 Flow Field Code

Since the flow field computation requires the most calculation time, a one-dimensional flow code is developed[14] for numerous geometrical and paramater variations. In case of the one-dimensional flow field modeling, the equation of state together with the continuity and Bernoulli equations yield the following expansion equations:

- inside the thruster (isothermal expansion):

$$\frac{\kappa}{\kappa-1}\frac{p_c}{\varrho_c}\left(\frac{\kappa-1}{\kappa}\ln\left(\frac{\varrho_c}{\varrho}\right)+1-\left(\frac{\varrho}{\varrho_c}\right)^{\kappa-1}\right)-\left(\frac{\dot{m}}{\varrho A}\right)^2=0 \tag{17}$$

- outside the thruster (adiabatic expansion):

$$v_{eo}^2+\frac{2\kappa}{\kappa-1}\frac{p_{eo}}{\varrho_{eo}}\left(1-\left(\frac{\varrho}{\varrho_{eo}}\right)^{\kappa-1}\right)-\left(\frac{\dot{m}}{\varrho A}\right)^2=0 \tag{18}$$

where v_{eo}, p_{eo} and ϱ_{eo} are the velocity, pressure and density of the plasma at the thruster nozzle exit.

For the description of the two-dimensional, axisymmetric flow, the following nonlinear hyperbolic system of differential equations with curvilinear, cylindrical coordinates is used:

$$\frac{\partial}{\partial t}\vec{q}+\frac{\partial}{\partial \xi}\vec{F}(\vec{q})+\frac{\partial}{\partial \eta}\vec{G}(\vec{q})+\vec{H}(\vec{q})=0 \tag{19}$$

The indices t, ξ, η indicate the partial differentiation with respect to time and to the ξ- and η-directions. The first three terms are used in the usual fluid dynamic manner, where $\vec{q}$ is the flow variables vector and $\vec{F}$ and $\vec{G}$ are the spatial derivatives vectors [15, 27]. The source vector $\vec{H}$ is developed to:

$$\vec{H}(\vec{q})=\begin{bmatrix} \rho v/r \\ \rho uv/r+\frac{\partial}{\partial \xi}\left\{\mu\left[2\frac{\partial U}{\partial \xi}+(\frac{\partial V}{\partial \xi}+\frac{\partial U}{\partial \eta})\right]\right\}+j_\eta B_\theta \\ \rho v^2/r+\frac{\partial}{\partial \eta}\left\{\mu\left[2\frac{\partial V}{\partial \eta}+(\frac{\partial U}{\partial \eta}+\frac{\partial V}{\partial \xi})\right]\right\}+j_\xi B_\theta \\ (p+e)v/r+\nabla\vec{q}_s-\sum_\nu n_\nu n_e \alpha_{e\nu}(T_h-T_e) \end{bmatrix}$$

The first terms in the source vector transform the plane two-dimensional- into a cylindrical calculation. The first additional terms in the impulse equations represent the stress tensor of the plasma flow, where the viscosity coefficient μ is given by [9]:

$$\mu=\frac{3}{8}\sqrt{\frac{\pi}{2}}\sum_l \frac{m_l n_l k T_l}{\sum_{\nu(=l)} n_\nu Q_{l\nu}\sqrt{m_{l\nu}kT_{l\nu}}} \tag{20}$$

Since the temperature of the heavy particles are equal, it is $T_l=T_{l\nu}=T_h$ and $m_{l\nu}$ is the reduced mass for l,ν as heavy particles subscripts. The last terms in the impulse equations represent the $\vec{j}\times\vec{B}$ forces. In the energy equation the second source vector term $\vec{q}_s$ represents the heat flux vector due to the heavy particles of the MPD flow, which is given by:

$$\vec{q}_s=\sum_l -\lambda_l\left(\frac{1}{2}\frac{T_l}{n_l}\nabla n_l+\nabla T_l\right) \tag{21}$$

The heat conductivity coefficients are given by:

$$\lambda_l=\frac{15}{8}\sqrt{\frac{\pi}{2}}\frac{n_l k^2 T_l}{\sum_{\nu(=l)} n_\nu Q_{l\nu}\sqrt{m_{l\nu}kT_{l\nu}}} \tag{22}$$

The transfer of Joule's heat is contained in the temperature compensation between the electron and the heavy particles temperature, which is represented by $\Sigma n_\nu n_e \alpha_{e\nu}(T_e-T_h)$ in the equation of energy conservation. The transport coefficients are derived in a similar manner as in [16, 28] and more detailed derivations for the coefficients are described in [9, 21]. The cross sections $Q_{l\nu}$ for all coefficients are taken from the references [10, 12, 23, 24].

2.5 Discussion of Results

2.5.1 Nozzle–type MPD Thrusters

A main goal for developing tne code with a one-dimensional flow calculation was to obtain a design instrument which provides a fast insight into the current distribution within a continuously running MPD thruster. The next figures show the distributions of the main parameters calculated for three nozzle–type throat geometries (see Fig. 3). The DT2 geometry has the narrowest throat diameter of 24 mm, whereas the DT5 has a bigger throat diameter of 30 mm, and the DT6 thruster doesn't have a throat at all, but has a cylindrical part with a diameter of 36 mm from the cathode up to the beginning of the nozzle. With these three geometries it can be expected that at the DT2 thruster the highest values of current density, and thus the highest temperatures, occur in the nozzle throat. According to the experiences in [14, 17, 18, 26] in the DT2 thruster also the highest voltage is predicted.

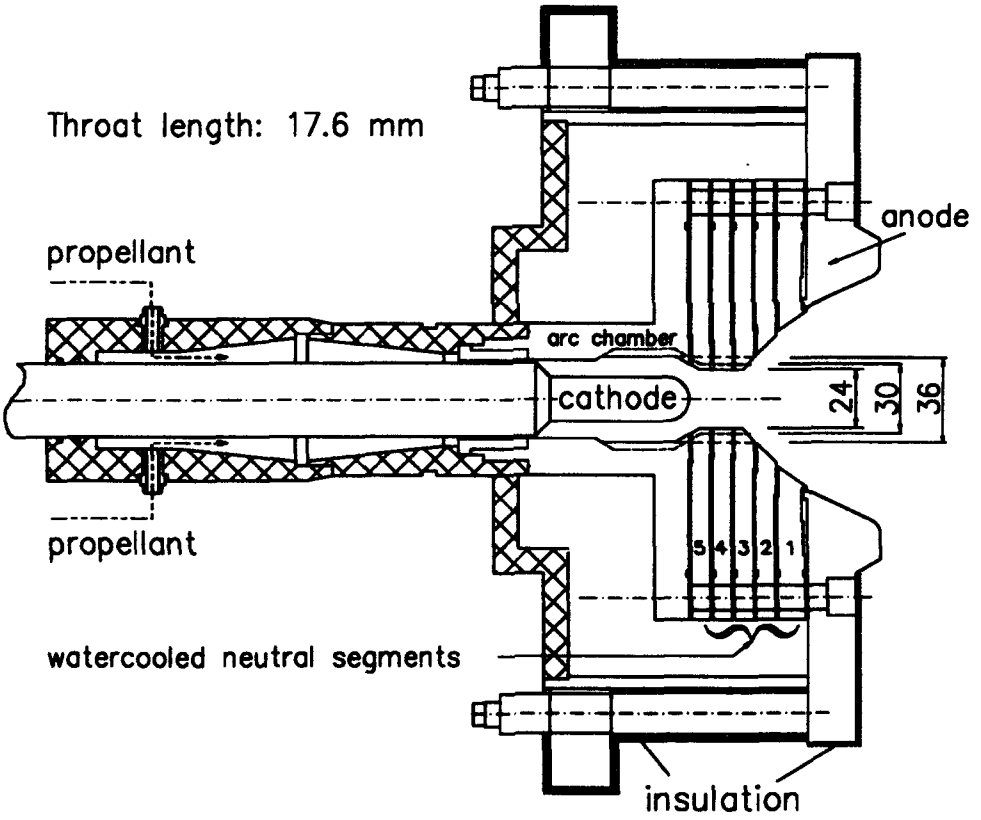

Figure 3: MPD thruster with modified throat geometries.

With quasi-steady pulsed thrusters it is possible to measure the current contour lines, but because of the high heat load of the probes it is not yet possible to compare these with experimental data on the continuously running thruster. This means there is a need for a calculation code in order to optimize steady state MPD thrusters. In Fig. 4 the calculated current contour lines are shown for the different throat geometries at 3000 A with a mass flow of 0.8 g/s argon.

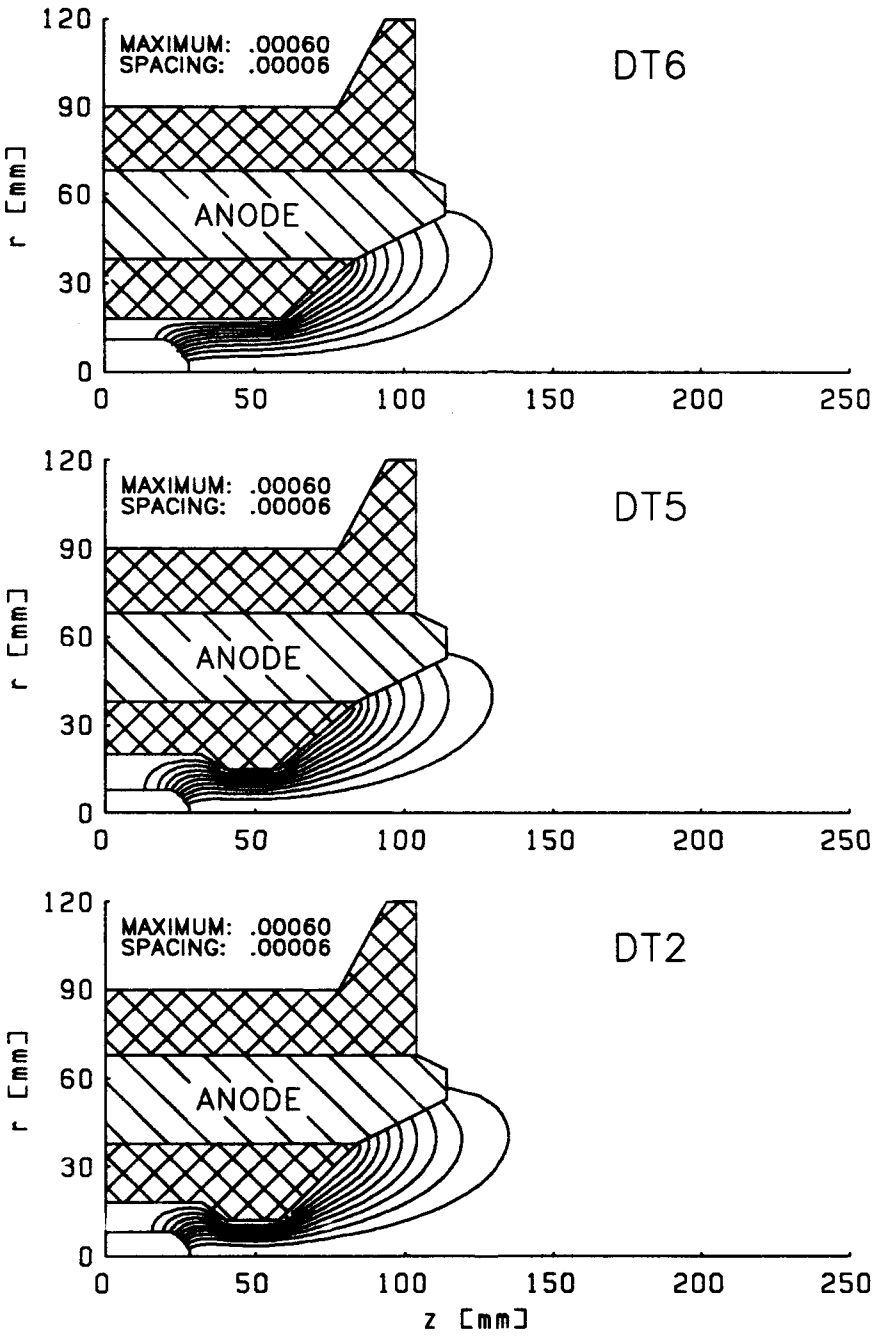

Figure 4: Current contour lines of the DT-geometries.

The electron temperature distribution within and outside the thruster at a current level of 2 kA is shown in Fig. 5. Against any expectation, the highest electron temperature is calculating for the DT6 thruster. This is due to the fact that the calculation which is necessary for the coupling of the electron and heavy particles, as described in equation 13, has not been considered due to numerical difficulties.

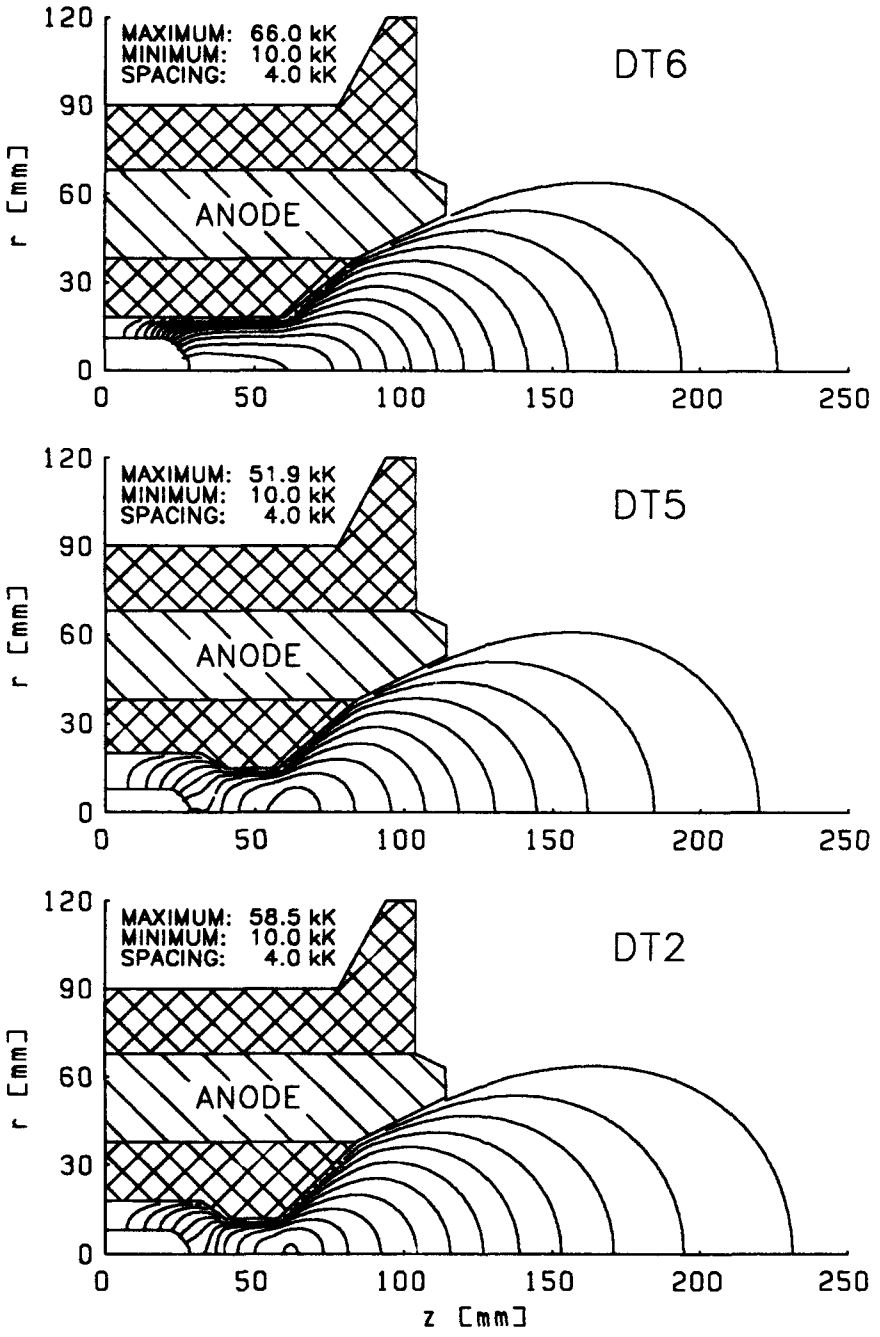

Figure 5: Electron temperature of the DT–geometries.

The potential lines within the discharge at 3 kA are plotted in Fig. 6. An integration across these lines yields the discharge voltage. As expected, the DT2 thruster has the highest and the DT6 thruster the lowest voltage value. This calculated discharge voltage is compared with the measured voltage in the current range between 1 and 5 kA in Fig. 8.

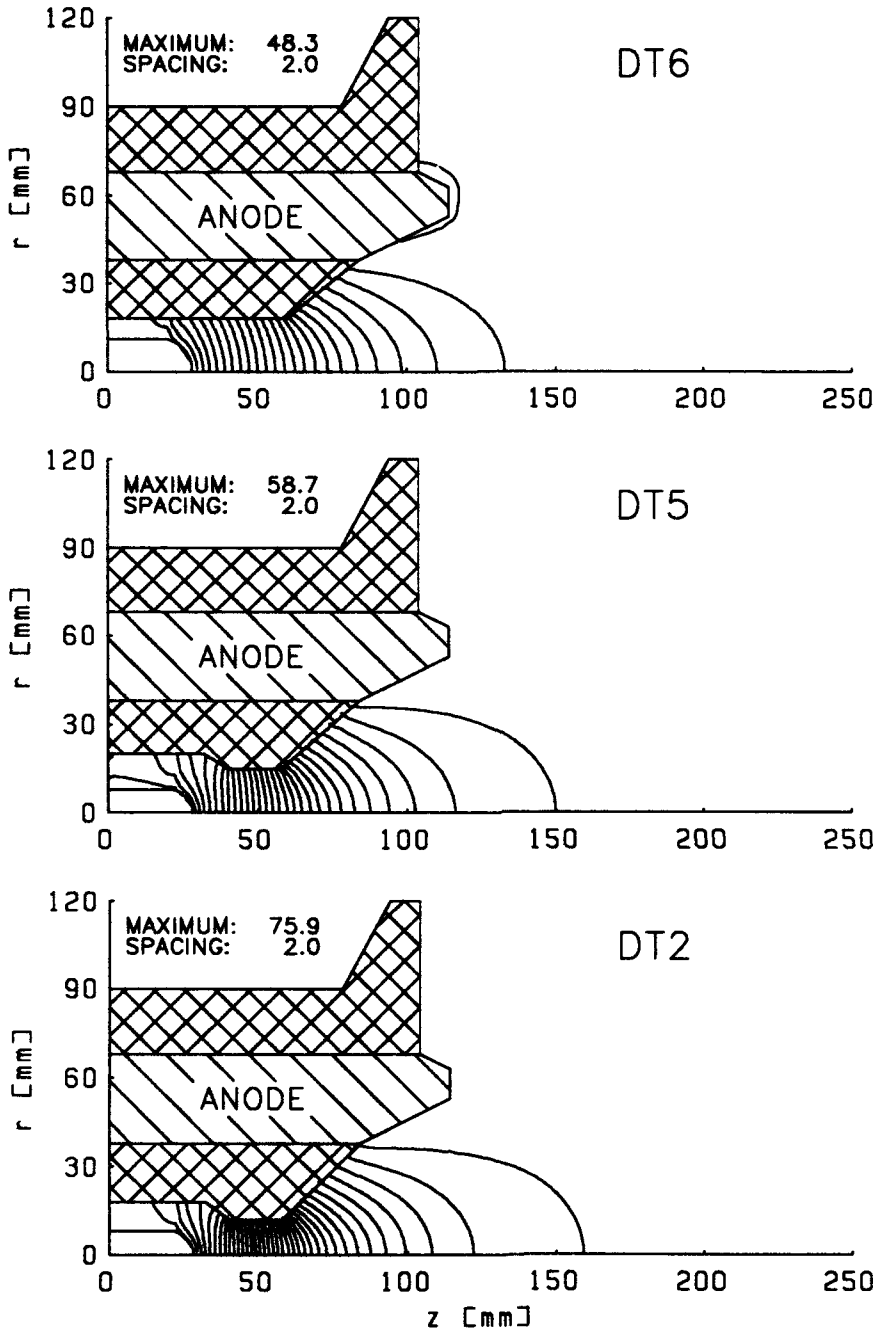

Figure 6: Potential lines of the DT–geometries.

Fig. 7 shows the ionization distribution of the argon plasma up to to the 5th ionization level. This ionization number shown here is calculated like the electron concentration in Fig. 2, with respect to the sum of the heavy particles to $\alpha = n_e / \sum_\nu n_\nu$. In comparison to the electron temperature one receives too high ionization values in the DT6 thruster according to the lacking coupling between the energy of the electrons and heavy particles.

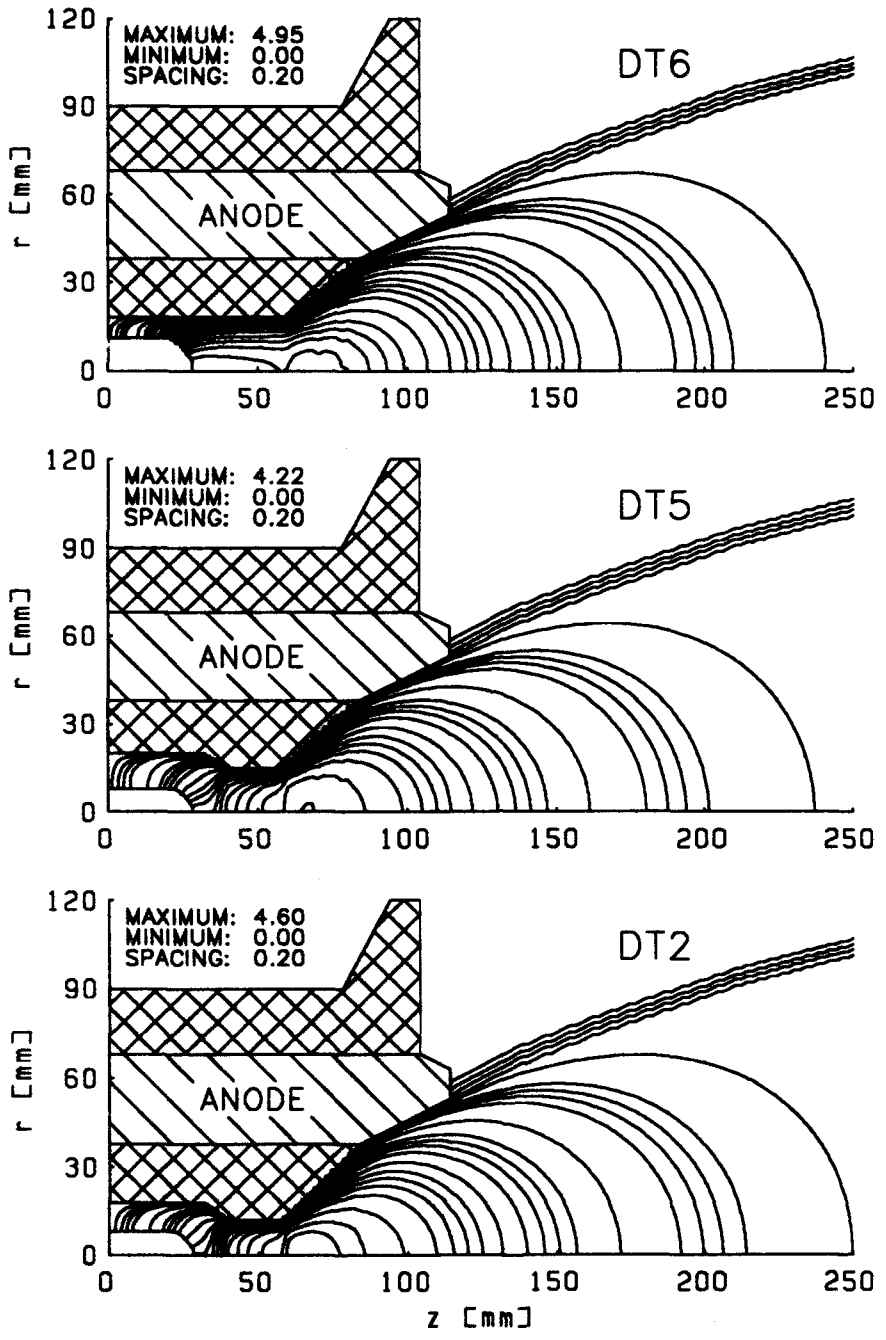

Figure 7: Ionization distribution of the DT–geometries.

The measured discharge voltages include, in contrast to the calculation, the electrode fall voltages. In the case of the cathode this voltage drop equals about the work function of the cathode material, which means with of thoriated tungsten between 1 and 3 volts, and is nearly independent of the discharge current. The anode fall voltage depends strongly on the current; starting with several negative volts at currents up to about 3 kA, the anode voltage rises steeply in the onset (unstable mod) region [1, 7].

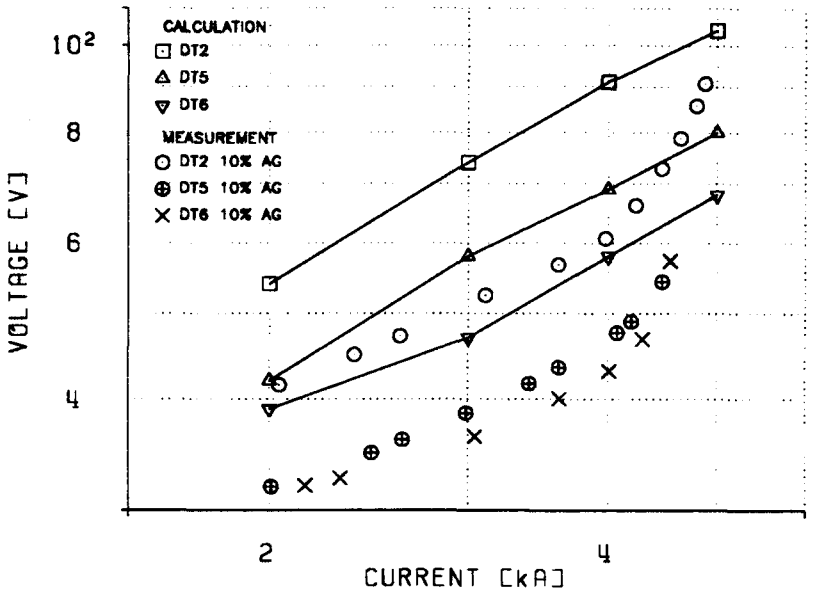

Figure 8: Calculated and measured discharge voltage.

According to the flow conditions and the known electromagnetic force configuration, the thrust can be calculated. The thrust of an MPD thruster is the sum of all gas dynamic surface forces and the electromagnetic volume forces. Hence it is

$$\vec{T} = \int_{A_s} \left(\varrho \, \overrightarrow{vv} + \overleftrightarrow{P} \right) \cdot d\vec{A} - \int_V \vec{j} \times \vec{B} \; dV \tag{23}$$

where A_s represents the surface of all internal walls and V is the current carrying volume.

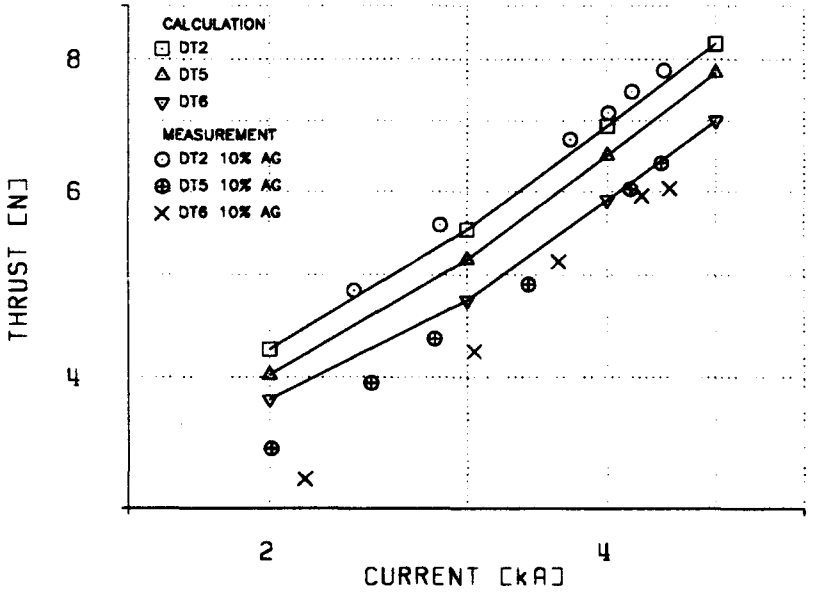

Figure 9: Calculated and measured thrust.

The calculated thrust is compared with experimental data in Fig. 9. For all thrusters with the three different geometries the calculated thermal thrust was verified with the thermal efficiency

from the experiment. The data shows a very good agreement specialy for the DT2 thruster for the complete presented current range.

The results for the DT2 and DT5 thrusters show a good correspondence with experimental values. The calculated results for the DT6 thruster show a bigger discrepancy to measured values because of the lacking coupeling between the electron and heavy particles energy. For this geometry a better correspondence to experimental values can be achieved by improving the one–dimensional flow model. Another possibility would be a two–dimensional flow modelling containing a comlete coupeling, like used for the ZT3 thruster, as presented in the next chapter, but then with a major increase of computation time.

2.5.2 Cylindrical MPD Thruster

The next figures show results for a cylindrical MPD thruster geometry, the ZT3–IRS (see Fig.10). Here the flow field was calculated by the Euler equations.

The flow inlet boundary conditions were iterated to coincide with an experimentally obtained cold gas thrust of 1 N at a mass flow rate of 2 g/s. For a given current of 6 kA the computation yields the current density distribution as illustrated in Fig. 11. The calculated current contour distribution corresponds with the current contour distribution at a continuing mode if the cathode is hot glowing and is emitting electrons thermionically along its complete length (see Fig.11).

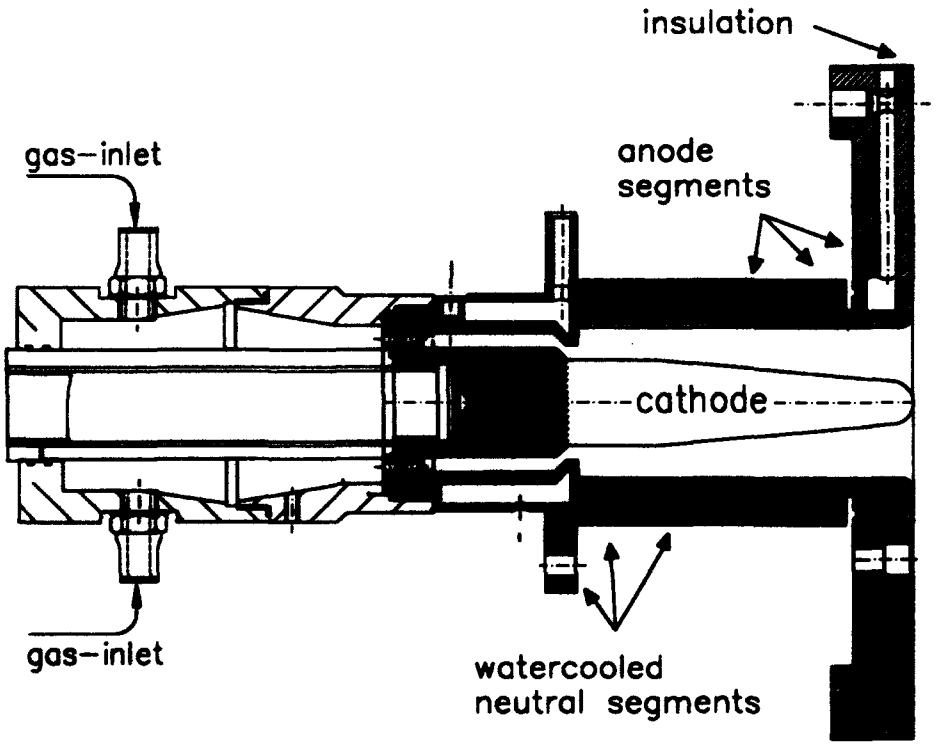

Figure 10: Cylindrical MPD thruster ZT3–IRS.

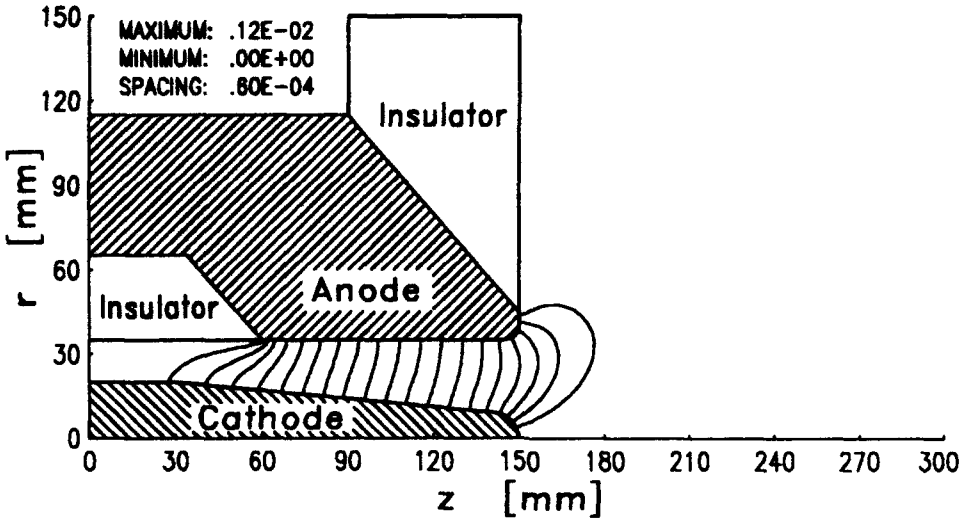

Figure 11: Calculated current contour lines.

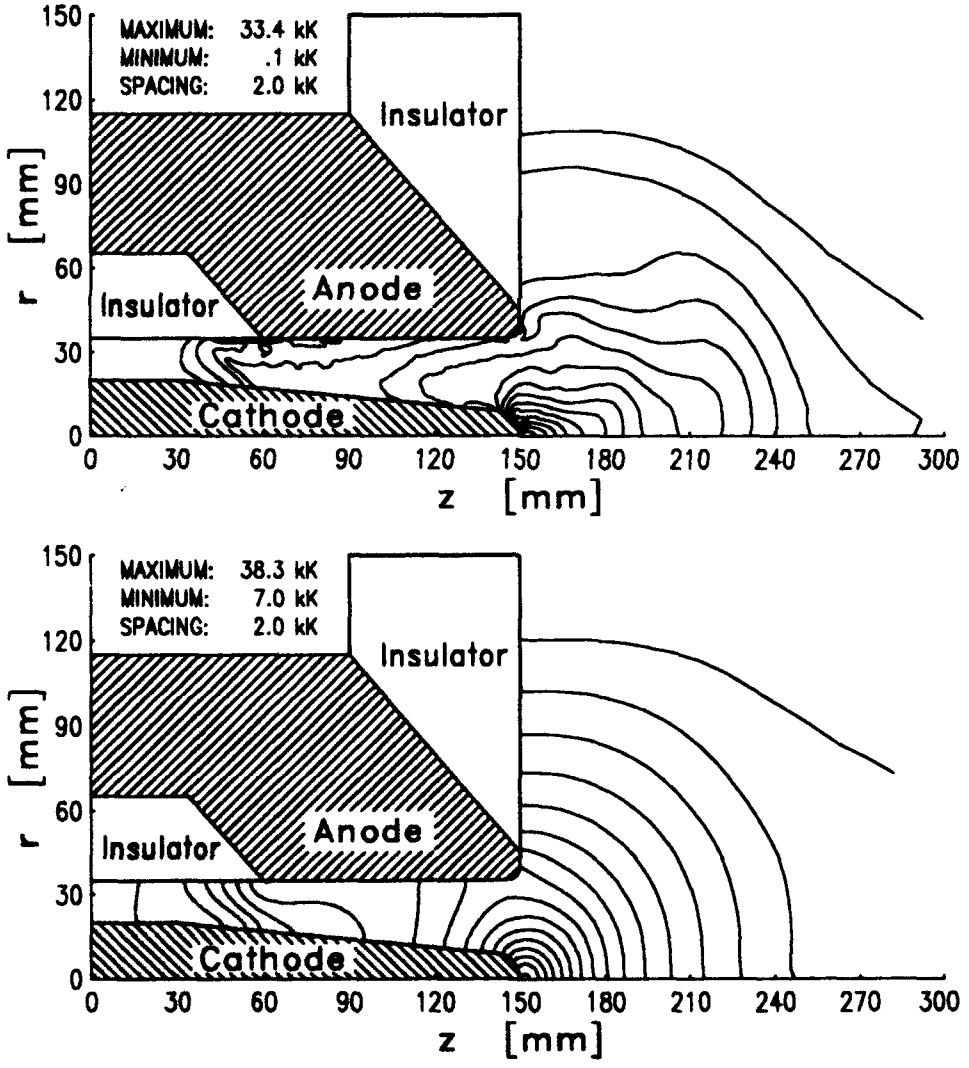

Figure 12: Heavy particles (top) and electron (bottom) temperature contours for 6 kA.

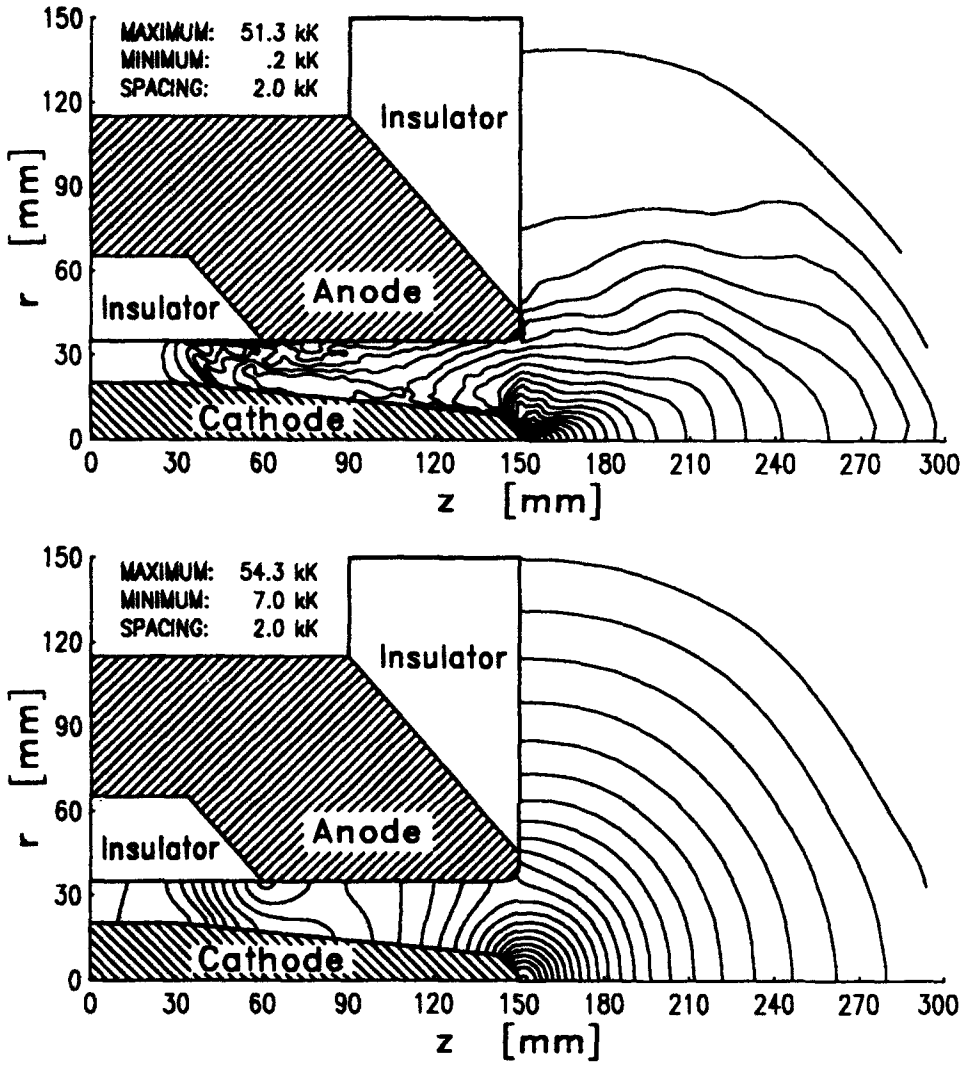

Figure 13: Heavy particles (top) and electron (bottom) temperature contours for 10 kA.

The heavy particle (top) and the electron temperature distribution (bottom) within and outside the ZT3 thruster is shown in Fig. 12 for a given current of 6 kA. The maximum temperature value of the heavy particles occurs at the tip of the cathode on the symmetry axis. The maximum electron temperature value occurs also at the tip of the cathode, but there is also a week increase of the electron temperature at the beginning of the anode.

In Fig. 13 the heavy particle (top) and the electron temperature distribution (bottom) is shown for a given current of 10 kA. The maximum temperature value of the heavy particles and the electrons is also at the tip of the cathode, but there is now a remarkable increase of the electron temperature at the beginning of the anode.

The pressure map (Fig. 14) demonstrates the expansion flow with the flow described in section 2.3, where the relatively low pinch effect was taken into account.

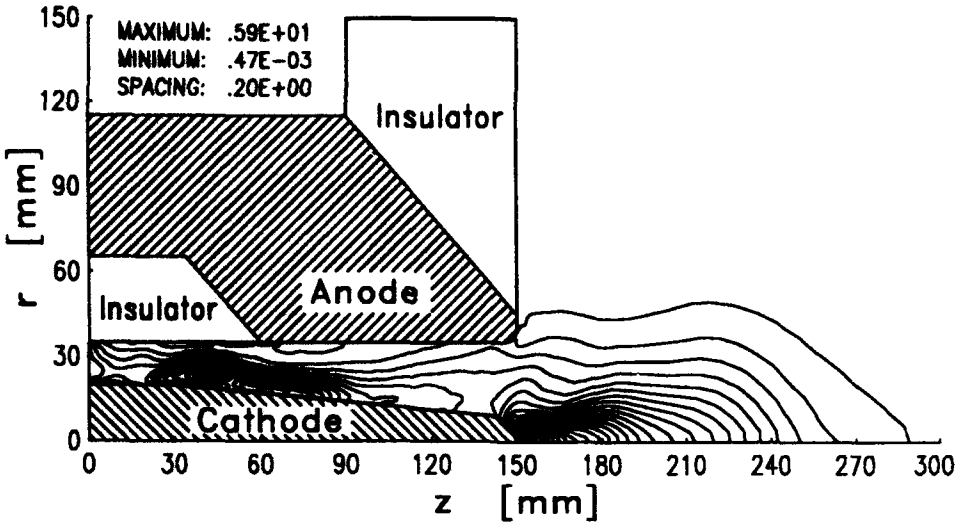

Figure 14: Pressure distribution.

The corresponding velocity distribution to the temperatures and density distribution is shown in Fig. 15 as a vector graph. It shows a high increase from the inflow boundary downstream. The radial velocity components inside the channel are quite small, which is also an indication for a relatively low pinch effect there.

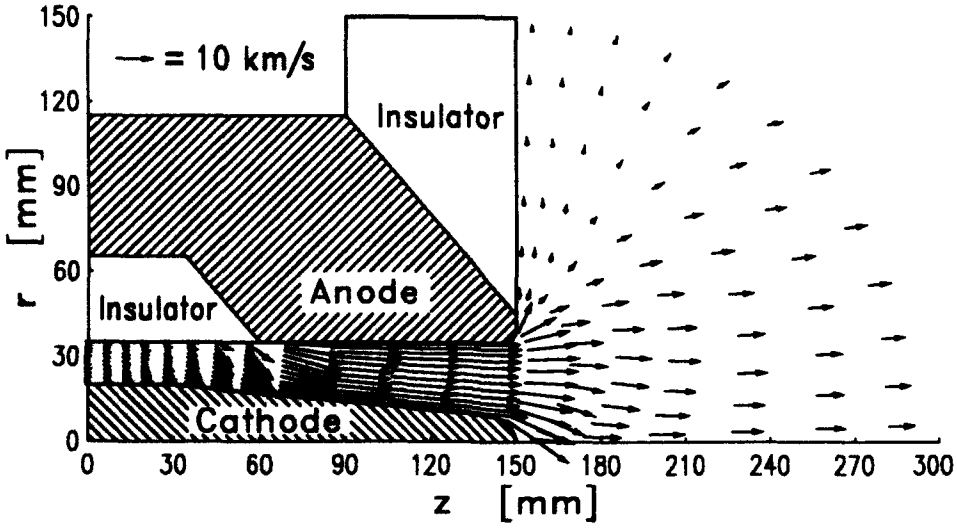

Figure 15: Velocity vector distribution.

The calculated thrust is 5.2 N for 4 kA, 8.1 N for 6 kA, 11.7 N for 8 kA, 16.4 N for 10 kA and 22.1 N for 12 kA. The measurements for the ZT3 thruster had not been finished by the time the report was completed.

2.6 Conclusions on Code Development

The codes described in this report were developed and tested in order to gain a more profound understanding of the fundamental processes occuring in MPD thrusters to predict thruster performances under various operating conditions and to end up with reliable design criteria.

The presented numerical analysis of an nozzle type MPD thruster was applied to rather complex geometries. Despite the shortcomingsof this code, namely the decoupled computation of the electromagnetic and flow equations, the one-dimensional flow model and the numerical difficulties concerning the energy-coupling between electrons and ions especially for thrusters with a large nozzle throat, it yields valuable results:

- Calculated integral values, such as thrust and discharge voltage fit the measured ones very well.
- The current patterns of the discharge coincide with the measured data fairly well.

Considering the saving in computation time this code is a useful design instrument.

The two-dimensional flow field calculation code with the curvilinear koordinates permits an improved simulation of geometry dependencies. This code was validated for the cylindrical thruster ZT3–IRS and showed good agreement with the experiments (Tab. 1) for the voltage and the current distribution on the three anode segments. Therefore in a later research period also the nozzle type thruster designs will be investigated with this two-dimensional curvilinear code.

3 Thruster Stability Investigation

One of the most critical limiting effects of the self-magnetic MPD-thrusters turns out to be the so called "Onset Phenomenon" [17, 18, 19, 20, 21] a plasma instability which causes severe degradation of the thruster performance at high power levels. According to experimentals done with the steady state nozzle type thrusters (see Fig. 3) for a given flow rate the dc voltage rises steeply if one exceeds a critical current (see Fig. 16); simultanously voltage fluctuations can be observed the intensity of which grow rapidly by further increasing the current. This effect finally leads to a strong degradation of the thruster by locally overheading the anode and irreversibly damaging the device. Similar observations could be observed on pulsed thruster devices [18, 21, 24, 25]. However, for a pulsed thruster experiment a correct measurement of the effective mass flow is extremly difficult since in fact a quasi steady condition near the cathode attachment and especially of the plasma cold gas interface within the discharge chamber remains highly questionable.

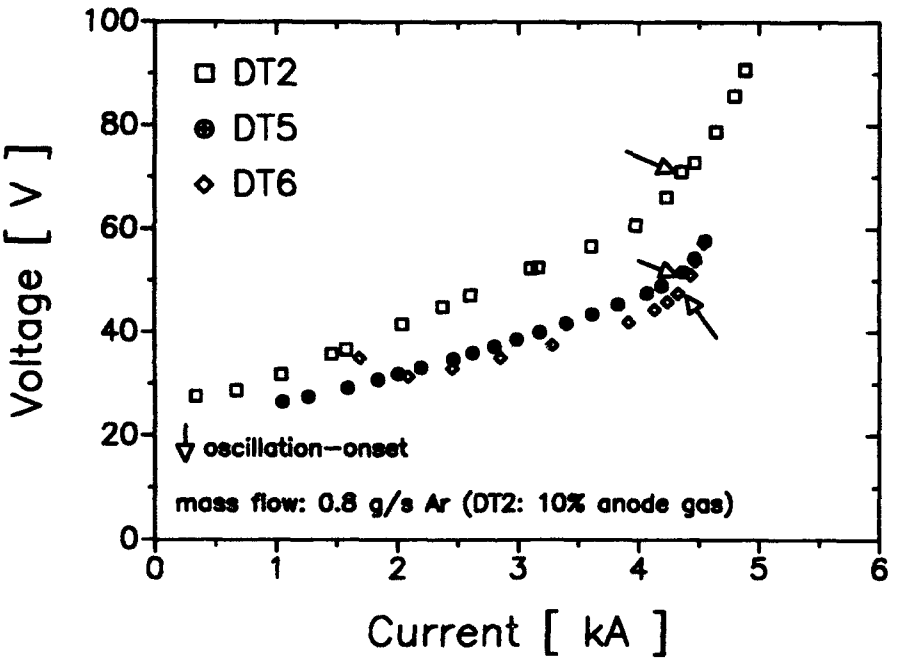

Figure 16: Voltage vs. current curve for a mass flow rate of 0.8 g/s of argon

Several different explanations [7, 8, 9, 10, 12, 13, 22, 23, 26, 27, 28, 29] have been put foreward so far and for most of them their analytical results agree fairly well with experimental observations. In this report a new explanation of the 'Onset-Phenomenon' is presented which is based on a 'run away Joule heating' mechanism of the current carrying plasma channel. This explanation is in excellent agreement with the experimentally found onset conditions measured on our continously running nozzle type thruster devices and therefore worth to be mentirned.

It is based on the '$\omega_e\tau_e$-dependency' of the electron heatflux (ω_e = cyclotron frequency of electrons, τ_e = average collision time) and the fact that with increasing $\omega_e\tau_e$ a contraction and overheating of the discharge channel may occur. Such a process consequently would lead to a 'run away heating' effect and as shown elsewhere [14, 30] to an instability of the rotationally symmetrical channel configuration. Based on this stability theory the new quasi stable configuration of the constricted discharge channel assumes a helical shape.

3.1 Run Away Heating Process

Within the constrictor or nozzle throat of a self magnetic MPD-thruster the plasma conditions are characterized by an axial flow at Mach 1 and the fact that the Joule heat input, due to the axial electric current which primarily heats up the electron gas is balanced by the radial conduction heat flux of the electrons and by the energy transfer to the heavy particle components. Since the pressure in those devices is well below 1 bar, one can neglect radiation losses and moreover may assume that the rotationally symmetric discharge column fills up the entire constrictor. If the pressure or the mass flow would become too high (arcjet conditions) the cold gas region between discharge column and constrictor wall, and hence the axial convection effects in the transition regime between outer arc column and cold gas should be accounted for. The governing equation of the constrictor follows now by the simplified energie equation of the electrons (see eq.(13)) as

$$\frac{j^2}{\sigma} = -\frac{d}{dr}\left(r\lambda_e \frac{dT_e}{dr}\right) + \sum_{\nu(\neq e)} n_e n_\nu \alpha_{e\nu} (T_e - T) \tag{24}$$

Now, within the discharge the conduction heat flux of the heavy particle components is approximately a factor $\sqrt{\frac{m_e}{m_\nu}} = 3,7 \cdot 10^{-3}$ smaller than that of the electrons. One can therefore propose that within the downstream area of the constrictor the heavy particles assume the temperature of the directly Joule heated electrons. Consequently in the downstream area of the constrictor the second term on the right site of equation (24) may be neglected. The solution of the remaining equation yields the following electron temperature profile [5].

$$T_e = \hat{T}_e \left\{1 - \frac{(n+1)^2}{n(n+4)}\left(\frac{r}{r_c}\right)^2 \left[1 - \frac{4}{(n+2)^2}\left(\frac{r}{r_c}\right)^n\right]\right\}^{\frac{2}{7}} \tag{25}$$

where

$$\hat{T}_e = 1.513 \cdot 10^2 J_0 \gamma \left(\frac{I}{r_c}\right)^{\frac{2}{5}} \tag{26}$$

is the maximum electron temperature at the center line degree Kelvin if $\frac{I}{r_c}$ is given in $\left[\frac{A}{m}\right]$. A stands for the electric current which is transported through the plasma column of radius r_c. This column radius is taken to be identical to the constrictor radius. The temperature profile has been derived as a solution of the electron-energy equation, (eq. (24) with $T_e = T$), by modeling the current density j through a paraboloid of grade n.

$$j = \hat{j}\left\{1 - \left(\frac{r}{r_c}\right)^n\right\} \tag{27}$$

where the maximum current density follows by the relation

$$\hat{j} = \frac{n+2}{n}\frac{I}{\pi r_c^2} \tag{28}$$

The product of the two factors J_o and γ in eq.(26) is a dimensionless number between about one and three. Herein the factor J_0 turns out to be a function of grade n of the current density paraboloid. In Table 1 J_0 is given for various values of n.

Table 1: J_0 (n)

n=	1.5	2	3	4	10	100
J_o =	1.297	1.246	1.185	1.149	1.070	1.008

The dimensionless factor J_0

The factor γ depends on the type of gas and is dimensionless, slowly varying function of $\hat{T}_e$ and the pressure p, or of $\frac{I}{r_c}$ and p within the constrictor for an argon plasma. This factor, γ, can be presented by [5]

$$\gamma_A \simeq \frac{0.853}{1 - 0.00189\left[1 - 0.22 \cdot ln\left(\frac{p}{10^5}\right)\right] J_0 \left(\frac{I}{r_c}\right)^{\frac{2}{5}}} \tag{29}$$

Here $\frac{I}{r_c}$ must be taken in $\left[\frac{A}{m}\right]$ and p in $[Pa]$. Equation (29) is valid within a pressure range of $10^3 Pa \leq p \leq 10^5 Pa$ and an $\left(\frac{I}{r_c}\right)$ -range of $5 \cdot 10^4 \frac{A}{m} \leq \frac{I}{r_c} \leq 5 \cdot 10^5 \frac{A}{m}$, provided the maximum temperature, $\hat{T}_e$ stays within the lower and upper limit of 15000 K and 40000 K, respectively. The tolerated error within these ranges is then less than $\pm$ 5%.

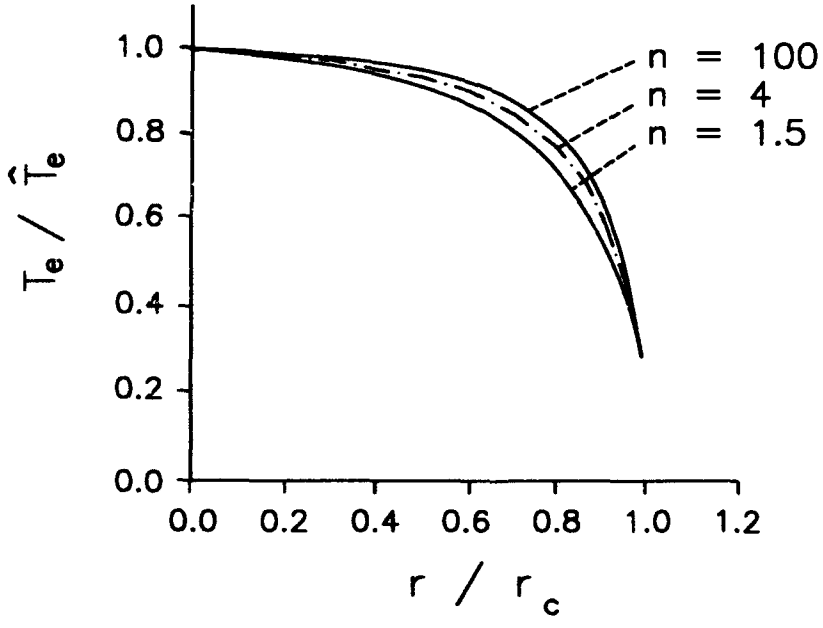

Figure 17: Temperature Profile for Different Grades n of the Current Density Paraboloides within the Arc Core

The dimensionless temperature profile according to eq.(25) is now plotted for various current densities or 'grades n' in Fig.17. As can be seen the temperature profile varies only slightly with n, a fact that justifies the method of solving the constrictor condition, i.e. by modeling the current density across the constrictor area.

So far the derived temperature profile was calculated on the assumption that no magnetic field effects are present or of importance. As it is known, however, within and around the current carrying arc column a self magnetic field or induction field $\vec{B}$ is inducted pointing in the azimuthal or θ - direction (see Fig.18). Based on the current density profile of eq.(27) with eq.(28) the radial depensity of this azimuthal magnetic induction field is given by

$$\mid \vec{B} \mid = B_\theta \equiv B(r) = \frac{\mu_0}{r}\int_0^r jrdr = \frac{\mu_0}{2\pi}\frac{I}{r_c}\frac{n+2}{n}\frac{r}{r_c}\left[1 - \frac{2}{n+2}\left(\frac{r}{r_c}\right)^n\right] \tag{30}$$

according to Maxwell's equation in the integral form.

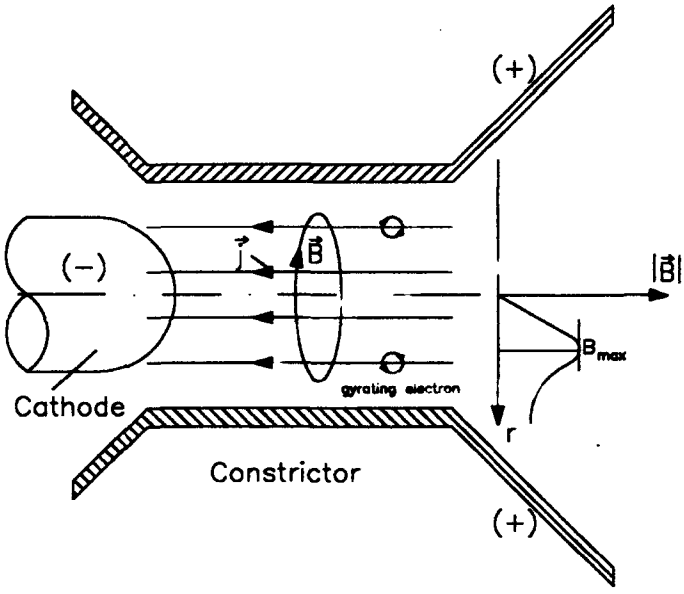

Figure 18: Illustration of the Self Magnetic Field within a Plasma Thruster

As a consequence of this azimuthal magnetic field which is normal with respect to the radial temperature and density gradients, the radial heat flux especially that due to electrons will be affected. Based on a rigorous gas kinetic perturbation approach which takes into account such a megnetic field [5] , it can be shown that the heat conduction coefficient as given by eq.(15) must be corrected by a tensorial factor which depends on the product of the cyclotron frequency ω_e and the average collision time of an electron τ_e. Now it is

$$\omega_e = \frac{eB}{m_e} \tag{31}$$

directly proportional to the magnetic induction field B, and the average collision time as gas kinetic expression given by [5]

$$\tau_e = \frac{8}{3}\sqrt{\frac{\pi}{2}}\frac{1}{\sum_{\nu(\neq e)} n_\nu Q_{e\nu}\frac{\sqrt{m_\nu k T_\nu}}{m_e+m_\nu}} \sim \frac{T_e^{\frac{5}{2}}}{p} \tag{32}$$

Within a magnetic field the heat conduction coefficient therefore becomes a tensor which follows by

$$\overleftrightarrow{\lambda}_i = \lambda_i \begin{vmatrix} \frac{sin\omega_i\tau_i}{\omega_i\tau_i} & -\frac{1-cos\omega_i\tau_i}{\omega_i\tau_i}\frac{B_z}{B} & \frac{1-cos\omega_i\tau_i}{\omega_i\tau_i}\frac{B_y}{B} \\ \frac{1-cos\omega_i\tau_i}{\omega_i\tau_i}\frac{B_z}{B} & \frac{sin\omega_i\tau_i}{\omega_i\tau_i} & -\frac{1-\omega_i\tau_i}{\omega_i\tau_i}\frac{B_x}{B} \\ -\frac{1-cos\omega_i\tau_i}{\omega_i\tau_i}\frac{B_y}{B} & \frac{1-cos\omega_i\tau_i}{\omega_i\tau_i}\frac{B_x}{B} & \frac{sin\omega_i\tau_i}{\omega_i\tau_i} \end{vmatrix} \tag{33}$$

where now $B_z = 0$, $B_y = -B$, $B_x = 0$ and $\omega_i = \frac{z_i eB}{m_i} = -\frac{eB}{m_e}$ for $i = e$. Since within the constrictor only a radial temperature gradient - i.e. parallel to the x-direction (see Fig.18) - is present the conduction heat flux vector, $\vec{q}_e$, of the electrons now becomes

$$\vec{q}_e = -\lambda_e \left\{ \frac{sin\omega_e\tau_e}{\omega_e\tau_e}\vec{u}_r - \frac{1-cos\omega_e\tau_e}{\omega_e\tau_e}\vec{u}_z \right\} \frac{d}{dr}T_e \tag{34}$$

where $\vec{u}_r$ and $\vec{u}_z$ are the unit vectors in the r- and z- direction, respectively. If the self magnetic field ($B \sim \omega_e\tau_e \neq 0$) is accounted for, the heat flux vector not only has a radial component but also an axial one. However, this axial heat flux does not lead to a net heat loss within the constrictor since, "what flows axially out flows axially in". Yet, the radial heat flux would lead to a net heat loss if it were not steadily compensated by Joule heating. This radial head flux now depends on the magnetic field and/or on the product of cyclotron frequency and the average collision time, $\omega_e\tau_e$, according to the factor

$$\frac{sin\omega_e\tau_e}{\omega_e\tau_e} \approx 1 - \frac{(\omega_e\tau_e)^2}{6} + \frac{(\omega_e\tau_e)^4}{120}\cdots \tag{35}$$

For very small $\omega_e\tau_e$ -values ($\omega_e\tau_e < 0.1$) this factor differs only by a negligible amount (-0.002) from one. The magnetic field effect can therefore be neglected as long as $\omega_e\tau_e < 0.1$. If however $\omega_e\tau_e$ exceeds a critical value, $(\omega_e\tau_e)_{crit}$ ($\approx 0.5\cdots 1.0$), this factor eq.(35) becomes noticeably smaller than one and the magnetic field effect on the radial heat conduction of the electrons must be accounted for. As one may realize, a noticeable reduction of the radial heat conduction consequently leads to a temperature increase within the core of the discharge channel.

Since now the self magnetic field B(r) and the electron cyclotron frequency ω_e have a maximum at a given radius r_M, according to (see eq.(30)) the optimization rule

$$\frac{dB(r)}{dr} = \frac{d\omega_e}{dr} = 0$$

the electron experimence the strongest megnetic field and have the highest cyclotron frequency, ω_e at the radius of

$$r_M = r_c\left(\frac{1}{2}\frac{n+2}{n+1}\right)^{\frac{1}{n}} \tag{36}$$

Therefore inside a radius of about r_M the heat conduction losses will decrease at first and simultaneously increase the temperature. However, with increasing temperature the collision frequency of the electrons (see eq.(14)) rises to such an extent that $\omega_e\tau_e$ increases even further and the conduction heat loss of the electrons are almost turned off. The consequence is a run-away heating within the channel core ($r < r_M$) until a new balanced condition is achieved. This new condition may be characterized by the fact that the radial conduction loss due to electrons ceases ($\omega_e\tau_e = \pi$) or is negligible and that the Joule heat -put into the electrons- is balanced by the energy transfer to the heavy particles. This energy is then compensated by the heat conduction loss of the heavy particles. The new temperature profile should therefore be determinated by the much smaller heat conduction losses of the heavy particles than by the classical electron conduction losses. Nevertheless, based on this discussion it may be concluded that if $\omega_e\tau_e$ taken at a radius of r_M exceeds a critical value of $(\omega_e\tau_e)_{crit} \approx 0.5 \cdots 1.0$, the temperature profile should increase in the core region ($r < r_M$) and decrease outside ($r > r_m$), causing a contraction of the discharge cross section (see Fig. 19).

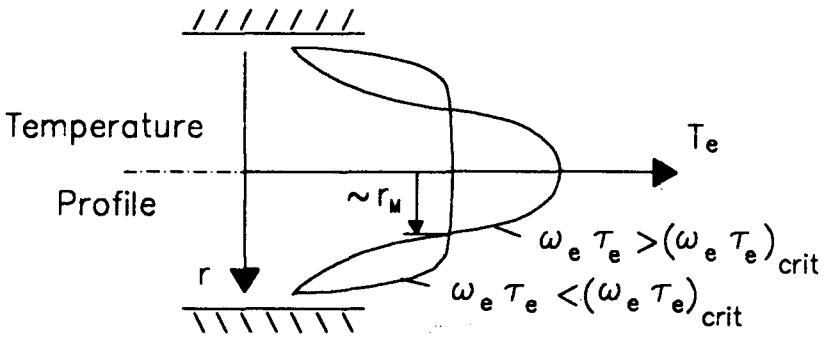

Figure 19: Illustration of the $\omega_e\tau_e$ -effect on the temperature profile

3.2 Calculation of $(\omega_e\tau_e)_{r_M}$

One now obtains according to eq.(31) and eq.(30) the cyclotron frequency at $r = r_M$ (see eq.(36)) by

$$\omega_e(r_M) = \omega_{eMax} = \frac{e}{m_e}\frac{\mu_0}{2\pi}\frac{I}{r_c}J_3 \tag{37}$$

where

$$J_3 = \left(\frac{1}{2}\right)^{\frac{1}{n}}\left(\frac{n+2}{n+1}\right)^{\frac{n+1}{n}} \tag{38}$$

is a function of the grade n of the current-density paraboloid (eq.(27)). J_3 varies between 1,1 and 1,0 if n changes from 1,5 to 100, respectively.

The collision time according to eq.(32) can now be rewriten in the form

$$\tau_e = \frac{3}{4}\sqrt{\frac{\pi}{2}} \frac{1}{n_e Q_{ee} \sqrt{\frac{kT_e}{m_e}} \left[1 + 2\sum_{\nu(\neq e)} \frac{n_\nu Q_{e\nu}}{n_e Q_{ee}} \sqrt{\frac{m_e T_\nu}{m_\nu T_e}}\right]} \tag{39}$$

where Q_{ee} follows by the Gvosdover cross section with $z_\nu = z_e = -1$. In the denominator of eq.(39) the sum with the terms proportional to $\sqrt{\frac{m_e T_\nu}{m_\nu T_e}}$ next to one can now be neglected. ($m_e T_\nu \ll m_\nu T_e$; $\frac{n_\nu Q_{e\nu}}{n_e Q_{ee}} < 1$ as long as one does not consider plasmas of a low degree of ionization, i.e. low temperatures ¡ 10000K). Together with eq.() one therefore obtains

$$\tau_e \simeq \frac{24\sqrt{2}\pi^{\frac{3}{2}}}{ln\left\{1 + 72\pi^2 \frac{\varepsilon_0^3 k^3 T_e^3}{n_e e^6}\right\}} \frac{\varepsilon_0^2 \sqrt{m_e}}{n_e e^4} (kT_e)^{\frac{3}{2}} \tag{40}$$

By means of the definition of the degree of ionization

$$\alpha = \frac{n_e}{\sum_{\nu(\neq e)} n_\nu} = \frac{\sum_{\nu(\neq e)} z_\nu n_\nu}{\sum_{\nu(\neq e)} n_\nu} \tag{41}$$

and the pressure relation

$$p = \sum_{\nu(\neq e)} n_\nu kT + n_e kT_e \tag{42}$$

the electron density can be expressed by

$$n_e = \frac{\alpha}{1+\alpha} \frac{p}{kT_e} \tag{43}$$

if constrictor conditions with $T_e \approx T$ are assumed. On replacing the electron density n_e in eq.(40) by eq.(43), the average collision time follows as a function of T_e and p.

$$\tau_e = \frac{24\sqrt{2}\pi^{\frac{3}{2}}}{ln\left\{1 + 72\pi^2 \frac{1+\alpha}{\alpha} \frac{\varepsilon_0^3 (kT_e)^4}{e^6 p}\right\}} \cdot \frac{1+\alpha}{\alpha} \frac{\varepsilon_0^2 \sqrt{m_e}}{e^4} \frac{(kT_e)^{\frac{5}{2}}}{p} \tag{44}$$

$$\simeq \frac{3.80 \cdot 10^{-18}}{ln\left\{5.705 \cdot 10^{-3} \left(\frac{1+\alpha}{\alpha p}\right)^{\frac{1}{4}} T_e\right\}} \frac{1+\alpha}{\alpha} \frac{T_e^{\frac{5}{2}}}{p} \tag{45}$$

In order to obtain the collision time at the effective channel radius r_M, one has to take for the electron temperature in eq.(45) $T_e = T_e(r_M)$. This temperatrue follows according to eq.(25) and (36) by

$$T_e(r_M) = \hat{T}_e \left\{1 - \frac{(n+2)(n+3)}{(n+1)(n+4)} \left(\frac{1}{2}\frac{n+2}{n+1}\right)^{\frac{2}{n}}\right\}^{\frac{2}{7}} \equiv \hat{T}_e J_2 \tag{46}$$

where J_2 is a dimensionless factor of the order 0,6 which depends on the grade n. Inserted into eq.(45) one obtains the effective collision time by

$$(\omega_e \tau_e)_{rM} = 3.76 \cdot 10^{-8} f \frac{1}{p} \left(\frac{I}{r_c}\right)^2 \tag{47}$$

Herein the p must be taken in Pascal, I in *Ampère* and r_c in meter in order to obtain $(\omega_e \tau_e)_{rM}$ dimensionless. The factor f is of the order one, depending on the type of gas and is a slowly varying function of n,p and $\hat{T}_e$ or of n, p and $\frac{I}{r_c}$. It is

$$f = \frac{J_3 (J_2 J_0)^{\frac{5}{2}}}{ln\left\{5.705 \cdot J_2 \left(\frac{1+\alpha}{\alpha p}\right)^{\frac{1}{4}} \hat{T}_e\right\}} \frac{1+\alpha}{\alpha} \tag{48}$$

At lower temperatures, $T_e(r_M) = J_2 \hat{T}_e$, and higher pressures the degree of ionization may become fairly small ($\alpha \ll 1$) such that f would become quite large. This range, however, is not of interest here and would result in wrong f -values since the electron-atom collision were neglected in τ_e and the transport coefficients. The formula of (48) should therefore only be used for $\alpha > 0.6$.

It should be remarked here that eq.(47) has been derived under the assumption that the radial heat conduction is still not noticeably affected by the $\omega_e \tau_e$ -effects, i.e. the factor $\frac{sin\omega_e \tau_e}{\omega_e \tau_e}$ with which the radial conduction heat flux should be multiplied was simply assumed to be approximately equal to one (see previous section). Now for $(\omega_e \tau_e)_{rM} = 0.25$ the relative error in the heat flux calculation amounts to only 1% and even for $(\omega_e \tau_e)_{rM} = 0.75$ it is less than 10%. It may therefore be concluded that if $(\omega_e \tau_e)_{rM}$ stays somewhat below about 0.75, eq.(47) can be applied to determine $(\omega_e \tau_e)_{rM}$. On the other hand the $(\omega_e \tau_e)_{rM}$ -value calculated according to eq. (47) should never exceed a critical value, $(\omega_e \tau_e)_{crit}$ (< 0.75) in order to avoid run away heating and sudden temperature and current density concentration towards the center line of the constrictor. Instead of relating $(\omega_e \tau_e)_{rM}$ to the pressure p as given in eq.(47), p may be replaced by the mass flow rate, $\dot{m}$ of the thruster. Provided that the discharge fills the entire cross section of the constrictor (πr_c^2) the mass flow rate is obtained by

$$\dot{m}_c = 2\pi \int_0^{r_c} \rho v r dr \tag{49}$$

where ρ is the local density given by the relation (see also eq.(42))

$$\rho = \frac{p}{(1+\alpha)\frac{\mathcal{R}}{M_0} T} \tag{50}$$

where M_0 is the atomic weight of the propellant, $\mathcal{R}$ is the universal gas constant and $T\,(= T_e)$ is the temperature of the heavy particles and within the constrictor set equal to the electron temperature. The velocity v can be replaced by the local speed of sound under isothermal conditions and follows as

$$v = \sqrt{\left(\frac{\partial p}{\partial \rho}\right)_{T=const}} = \sqrt{(1+\alpha)\frac{\mathcal{R}}{M_0} T} \tag{51}$$

Hence, the axial mass flow through the constrictor can be calculated by

$$\dot{m}_c = 2\pi \int_o^{r_c} \frac{p}{\sqrt{\frac{\mathcal{R}}{M_0} T (1+\alpha)}} r dr \tag{52}$$

Neglecting the magnetic pinch effect - which is indeed allowed here - one obtains with n=4 for the mass flow rate

$$\dot{m}_c = \pi r_c^2 \cdot p \cdot \sqrt{\frac{M_0}{\mathcal{R}\hat{T}}} \frac{1.15}{\sqrt{1+\bar{\alpha}}} \tag{53}$$

where $\bar{\alpha}$ is an average degree of ionization which can be approximated by $\alpha\,[T_e\,(r_M)]$. If in eq.(47) the pressure p is now replaced according to the above relation of eq.(53), and $\hat{T} = \hat{T}_e$ by eq.(26), one obtains

$$(\omega_e \tau_e)_{rM} = 1.21 \cdot 10^{-10} \cdot f^* \cdot \sqrt{M_0} r_c^{\frac{1}{5}} \frac{I^{\frac{9}{2}}}{\dot{m}} \tag{54}$$

Herein I must be taken in [A], the mass flow rate $\dot{m}$ in [kg/s] and the arc constrictor radius r_c in [m] in order to obtain $(\omega_e \tau_e)_{rM}$ dimensionless. The factor f^* is related to f by

$$f^* = \frac{f}{\sqrt{J_0 \gamma}\sqrt{1+\alpha}} \tag{55}$$

where for $n \neq 4$ the relation must be considered as an approximation.

f^* now is a slowly varying function of T_e and p or of $\frac{I}{r_c}$ and p, or of $\frac{I}{r_c}$ and $\dot{m}$ according to eq.(53). In Fig.20 the factor f^* is plotted for argon (f_A^*), as a function of $\frac{I}{r_c}$ with the pressure as a parameter for n=4. One can see that within the ranges of interest ($2.6 \cdot 10^5 \frac{A}{m} < \frac{I}{r_c} \leq 4 \cdot 10^5 \frac{A}{m}$; $10^3 Pa < p < 10^4 Pa$) for both propellants f^* varies only very little and that within these ranges f^* can be approximated by a constant of about 0.40 with an error of about $\pm$ 0.06 for argon. Hence it is a fair approximation to replace (f^*) within eq.(54) by 0.40. The product of average cyclotron frequency and electron collision time at the radius r_M of the discharge channel where the self magnetic field becomes a maximum follows therefore by

$$(\omega_e \tau_e)_{rM} \simeq 0.50 \cdot 10^{-10} \sqrt{M_o} \cdot r_c^{\frac{1}{5}} \frac{I^{\frac{9}{5}}}{\dot{m}_c} \tag{56}$$

This approximate formula shows that the number $(\omega_e \tau_e)_{rM}$ is primarily proportional to the $\frac{9}{5}$ -th power of the current and inversely proportional to the mass flow through the discharge channel. With increasing channel or constrictor radius r_c, $(\omega_e \tau_e)_{rM}$ should also slowly increase; however, this effect is very weak since the r_c -dependency is only proportional to the $\frac{1}{5}-$ th power. The atomic weight dependency is proportional to the square root since within the discharge channel the molecules are dissociated. For argon as propellant $M_0 = 40$.

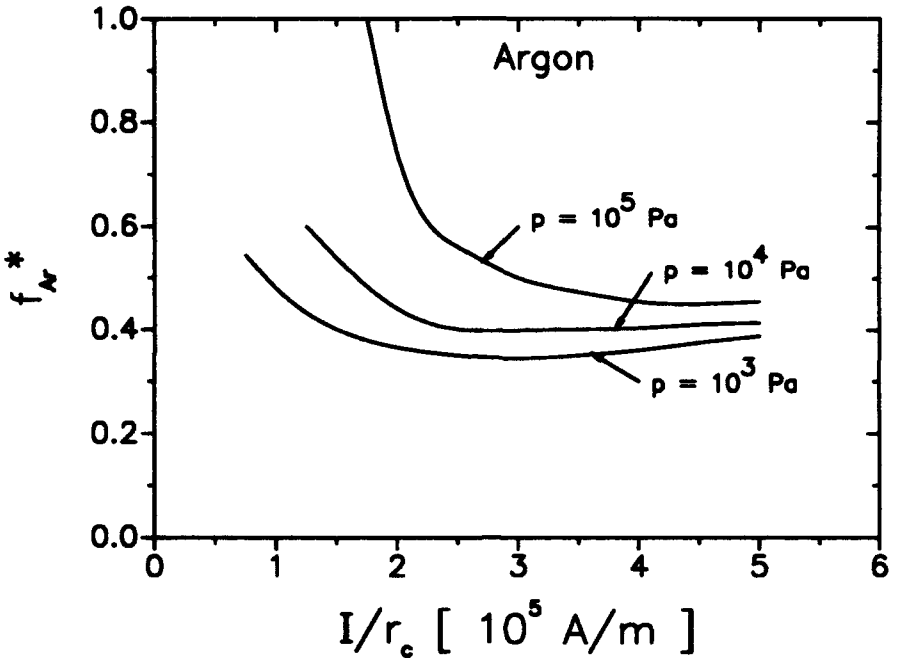

Figure 20: The factor $f^* = f_A^*$ for argon as a function of $\frac{I}{r_c}$ with p as a parameter

3.3 Experiment and Comparison with Calculations

As mentioned above the magneto-plasma-dynamic thruster reaches an unstable mode at high power levels. The experiments show that voltage versus current curve rises steebly above a certain current and that somewhat above this threshold voltage fluctuations occur the amplitudes of which increase dramatically until the thruster becomes irreversibly damage. The 'onset current' (I_{crit}) is now taken as that current at which the voltage noise becomes noticeable but at which the thruster is still not irreversibly damaged. The measured onset conditions so far are plotted in Table 2. Regarding the DT-2 thruster with a constrictor diameter of 24mm the onset conditions are covered between a mass flow rate of 0.3 g/s and 1.5 g/s. In the case of the DT-5-thruster with a constrictor diameter of 30mm, only two currents at a mass flow rate of 0.8 and 1.6 g/s have been measured with argon as propellant.

For the DT-6 thruster which had a cylindrical shape of constant cross sectional area for the arc chamber and the throat with a diameter of 36mm, the onset regime is couvered between a mass flow range of 0.8 g/s to 2.4 g/s argon. In the last experiment a current of 8300 A has been reached at only a faint voltage noise. In order to avoid thrusterdamage the current has not been increased further.

All these measurements are subtle since only a minor current increase beyond this onset can lead to a failure and total damage of the thruster. Especially at higher critical currents and mass flower rates one has to be extremely carefull to avoid local overheating of the anode.

Table 2: List of Available Onset Conditions for Different Thruster Types, with argon as propellant.

Type of Thruster (constrictor diameter)	Mass Flow Rate $\dot{m}_c$ [g/s]	Onset Current I_{crit} [A]
DT-2 (24mm)	0.3	2700
	0.6	3800
	0.8	4500
	1.0	4800
	1.5	6000
DT-5 (30mm)	0.8	4300
	1.6	6400
DT-6 (36mm)	0.8	4600
	1.2	5650
	1.6	6550
	2.0	7450
	2.4	$\geq$ 8300

More recent measurement with a CCD-camera which allows exposure times of 100 ns indicate that near onset conditions the discharge cannot be considered being rotational symmetric filling out the entire discharge chamber or nozzle of the thruster, but rather assumes a more confined channel configuration which moves around rapidly. On increasing the current only by a small amount above onset the anode attatchment tends to stick more and more to a local point thereby overheating and irreversibly damaging the anode at a confined spot (Fig. 21).

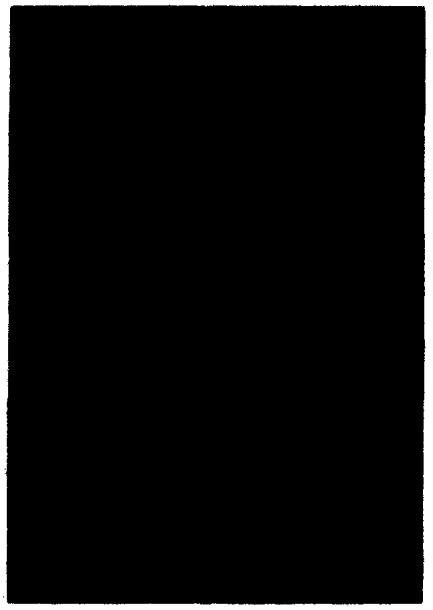

Figure 21: CCD–camera picture at onset condition

For the sake of comparison of the experiments with the analysis for all three thruster types (DT-2, DT-5 and DT-6) the onset conditions - I_{crit} as a function of $\dot{m}$ - following from eq.(54) were calculated according to the requirement

$$(\omega_e \tau_e)_{\tau M} = 7,65 \cdot 10^{-10} f^* r_c^{\frac{1}{5}} \frac{I^{\frac{2}{5}}}{\dot{m}_c} \leq (\omega_e \tau_e)_{crit} \tag{57}$$

with $(\omega_e \tau_e)_{crit}$ -values of 0.5 and 0.75. The results of these calculations are plotted as lines for the DT-2, DT-5 and DT-6 thrusters in Fig. 22, Fig. 23 and Fig. 24 respectively. Herein the factor f_A^* was determined for n=4 by accounting for the weak dependency of $\dot{m}$ and $\frac{I}{r_c}$. One can see that the measured points lie below the upper curve with $(\omega_e \tau_e)_{crit} = 0.75$ as could be expected and that the functional dependency of the onset condition for argon, given by

$$r_c^{\frac{1}{5}} \frac{I_{crit}^{\frac{2}{5}}}{\dot{m}_c} = 1.95 \cdot 10^9 \left[\frac{m^{\frac{1}{5}} A^{\frac{2}{5}}}{kg/s} \right] \tag{58}$$

are within the accuracy of experiment and theory ($\leq 10\%$) for both thruster types. According to this half empirical relation (eq.(58)) $(\omega_e \tau_e)_{crit}$ should be set equal to 0.62 for all three thrusters.

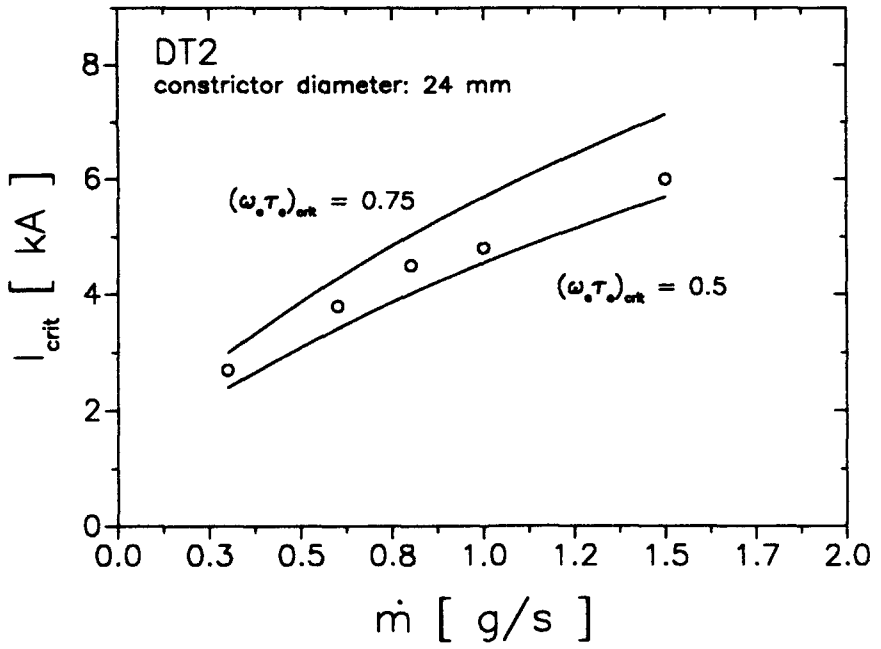

Figure 22: Critical current as a function of the mass flow rate (DT-2)

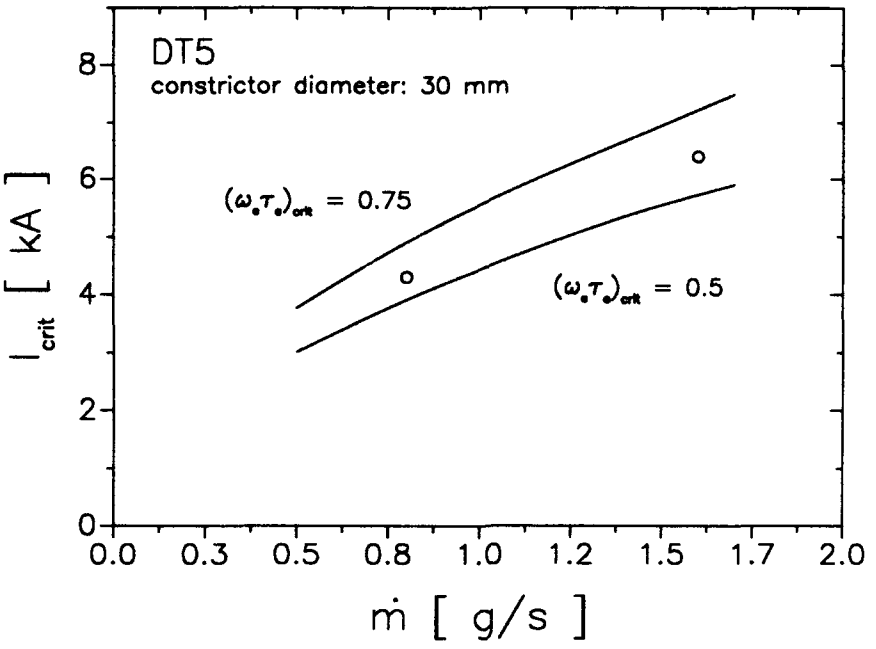

Figure 23: Critical current as a function of the mass flow rate (DT-5)

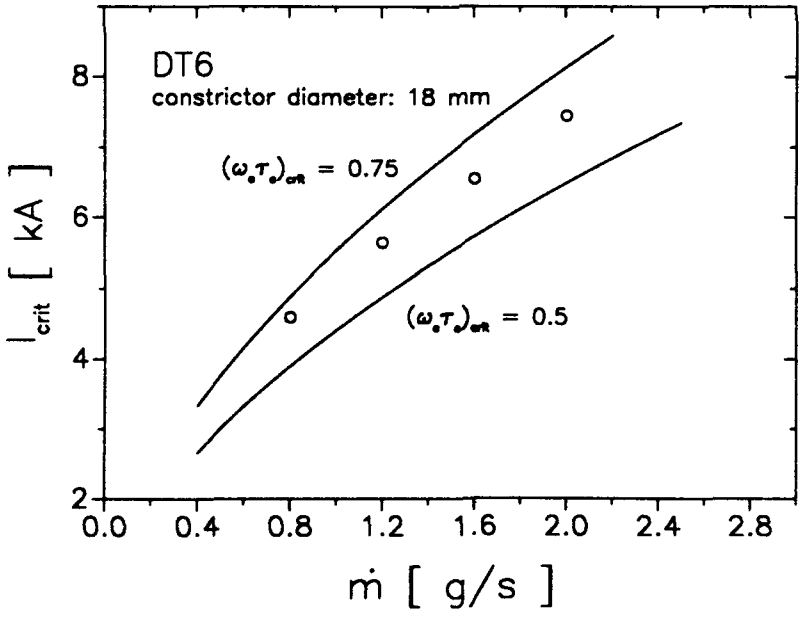

Figure 24: Critical current as a function of the mass flow rate (DT-6)

3.4 Stability Considerations

The previous sections have shown that 'onset' can be quantitatively explained by a dramatic decay of the radial heat conduction loss of the electrons caused by the azimuthal self magnetic field. When the product of cyclotron frequency and average collision time of the electrons exceeds a critical value ($(\omega_e\tau_e)_{rM} \geq 0.6$) a noticeable quenching of the heat conduction occurs leading to an electron temperature increase within the center of the discharge channel and therefore to a constriction of the electrically conducting channel. This run-away heating process in the discharge core proceeds until a new, energetically balanced discharge channel will have adjusted itself. This new adjustment is characterized by the fact that now the Joule heat is balanced by the heat conduction loss of the heavy particles. Since the conduction coefficient due to the heavy particles is smaller by a factor of $\sqrt{m_e/m_o}$ than that of the electrons without $\omega_e\tau_e-$ effect, the radial temperature slope should steepen and consequently lead to a temperature increase in the discharge channel core. This concentration of the discharge channel now causes a portion of the gaseous propellant to stream around the core and not through the actual current carrying channel. The mass flow $\dot{m}_c$ flowing through the discharge therefore decreases when the $\omega_e\tau_e-$ effect sets in $[((\omega_e\tau_e)_{rM} \geq 0.6)]$.

Now it shall be shown that this transition from a high to a low heat conduction or from a larger to a lower mass flow $\dot{m}_c$ and/or from a chamber filling to a more constricted discharge channel initiates the proper instability. So far only a straight rotational symmetric discharge configuration within the constrictor has been considered. However, when the onset occurs, a constricted discharge channel will also continue downstream into the diverging nozzle section where rotational symmetry can no longer be expected. Now in order to determine the new 'onset' channel configuration from the constrictor downwards to the anode ring a previously developed theory on arc stability [29, 32] will be applied. According to this theory the configuration of a current carrying plasma channel is only a stable one if a) the sum of all transverse acting forces per unit channel length ($\vec{\chi}_\perp$) is zero along the entire length of the discharge axis and b) if for any devitation $\left(\vec{\delta}\right)$ of such a balanced configuration a resultant force $\vec{\chi}_\perp \neq 0$ is initiated pointing in the opposite direction of the deviation, i.e. tends to bring the channel into its original balanced state.

For the problem considered here, this force accounting for all body- and surface forces (e.g. magnetic forces caused by the self magnetic field, friction, convection and pressure effects and if necessary coriolis and centrifugal forces) follows as [29]

$$\vec{\chi}_\perp = \left\{\frac{\mu_0}{8\pi}I^2\left[1+f(n)\right] - \int_{A_c}\rho v_z^2 dA_c + R\frac{d\gamma}{ds}v_{cy}\int_{A_c}\rho v_z dA_c\right\}\frac{\vec{R}}{R^2} \tag{59}$$

Now, R in eq.(59) is the local radius of curvature (see Fig. 25), $\vec{R}$ the vector pointing to the center of curvature in the x-direction, $f(n)$ is a slowly varying function of the grade n and is approximately equal to 0.8 and v_{cy} is the transverse velocity of the channel in the y-direction, i.e. normal to the axis (z-direction) and normal to $\vec{R}$ (see Fig. 25).

The quantity $\frac{d\gamma}{ds}$ is the so called "twist" of the channel and follows for the most general channel segment configuration, the conical helix (see Fig. 26) by

$$\frac{d\gamma}{ds} = \frac{1}{r_h}sin\beta\, cos\beta\sqrt{1 - tan^2\alpha\, tan^2\beta} \tag{60}$$

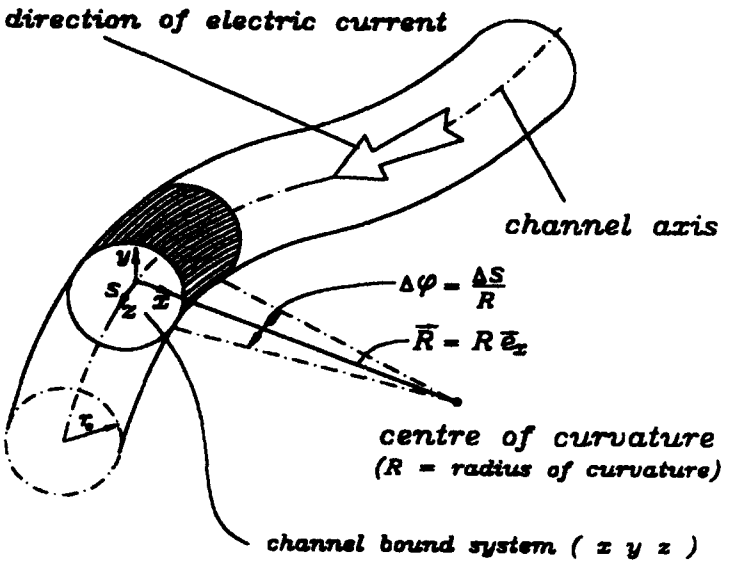

Figure 25: Arbitrarily shaped discharge channel configuration

Herein r_h is the local distance of the channel segment from the conus axis and called helix radius, β is the shape angle of the winding of the channel axis and α the half conus angle as shown in Fig.26.

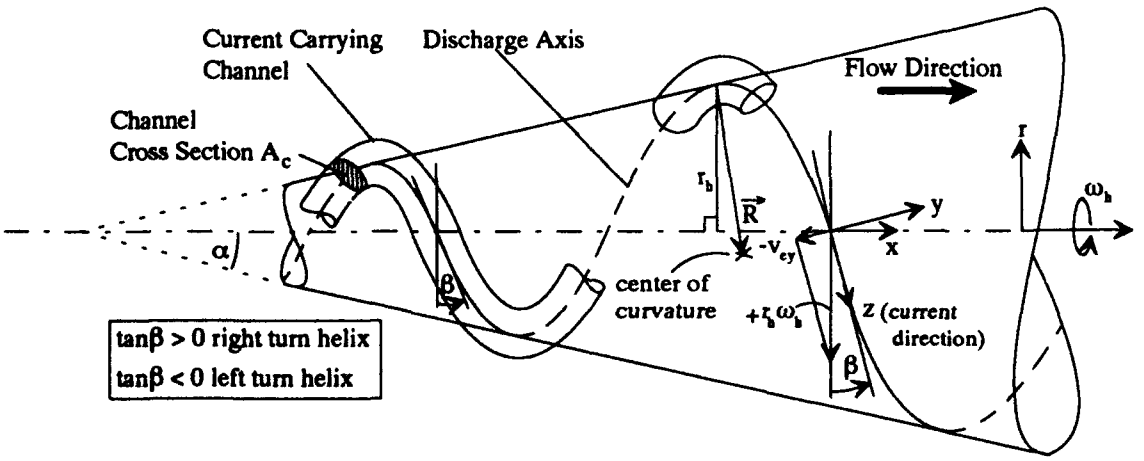

Figure 26: Right–turn Conical Helis of Constant β and α

For such a channel segment configuration the radius of currature, R, is now related to the helix radius r_h and the angles α and β by

$$R = \frac{r_h}{cos^2\beta\sqrt{1 - tan^2\alpha\, tan^2\beta}} \tag{61}$$

Now, the axial mass transport given by

$$\int_{A_c} \rho v_z dA_c = \pm \dot{m}_c \tag{62}$$

is positive if the mass flow along the channel axis is in the same direction as the electric current and negative if in the oposite direction.

According to geometrical considerations the transverse channel velocity, v_{cy}, can be related to the rotational frequency, ω_h, of the helix. It is

$$v_{cy} = -r_h \omega_h sin\beta \sqrt{1 + tan^2\alpha \, tan^2\beta} \tag{63}$$

Herein ω_h can be positive or negative depending on wether it is a right turn revolution with respect to the main helixal axis, z, or a left turn revolution with respect to z (seeFig.26). By means of the equations (60), (61), (62) and (63) the formula for the resultant transverse force, eq.(59), can now be written in the form

$$\vec{\chi}_\perp = \left\{ \frac{\mu_o}{8\pi} I^2 [1 + f(n)] - \int_{A_c} \rho v_z^2 dA_c - (\pm \dot{m}_c) \, r_h \omega_h sin\beta \, tan\beta \sqrt{1 + tan^2\alpha \, cos^2\beta} \right\} \frac{\vec{R}}{R^2} \tag{64}$$

If one now assumes that the axial speed v_z within the Joule heated channel reaches the speed of sound [see also eq.(53)] the axial impuls transport can be approximated by

$$\int_{A_c} \rho v_z^2 dA_c = 0,87 \sqrt{\frac{\mathcal{R}}{M_0} \hat{T} (1 + \alpha)} \; \dot{m}_c \tag{65}$$

or by replacing $\hat{T} = \hat{T}_e$ according to eq.(26) one obtains after some rearangements

$$\vec{\chi}_\perp = \frac{\mu_0}{8\pi} [1 + f(n)] \, \dot{m}_c \left(\frac{I}{r_c} \right)^{\frac{1}{5}} \left\{ \frac{I^{\frac{9}{5}}}{\dot{m}_c} r_c^{\frac{1}{5}} - \frac{1,95 \cdot 10^{10}}{1 + f(n)} \sqrt{\frac{\gamma J_0 (1 + \alpha)}{M_0}} \right.$$
$$\left. \mp \frac{2 \cdot 10^7}{1 + f(n)} \left(\frac{r_c}{I} \right)^{\frac{1}{5}} r_h \omega_h sin\beta \, tan\beta \sqrt{1 + tan^2\alpha \, cos^2\beta} \right\} \frac{\vec{R}}{R^2} \tag{66}$$

Herein I must be taken in [A]; r_c, R and r_h in [m], ω_h in $[s^{-1}]$ and the mass flow rate through the current carrying channel, $\dot{m}_c$ in $[kgs^{-1}]$ in order to obtain the resultant force per unit channel lenght in $[Nm^{-1}]$. Depending if the mass flow and the obtain current have the same or the opposite orientation one had to take the minus of the positive sign respectivly. If one applies this equation to the discharge flow of our MPD-thrusters, the electric current is opposite to the flow (if the anode is located downstream); therefore the plus sign in eq.(66) is valid. On the other hand β must fall in the range $-\pi < \beta < 0$ (*or* $\pi < \beta < 2\pi, 3\pi < \beta < 4\pi, etc.$) such that $sin\beta < 0$. Taking a current-density paraboloid of grade n=4 and argon as propellant with an atomic weight $M_o = 40$, the transverse force per unit channel lenght becomes proportional to

$$\vec{\chi}_\perp \sim \left\{ \frac{I^{\frac{8}{5}}}{\dot{m}_c} r_c^{\frac{1}{5}} - 1,7 \cdot 10^9 \sqrt{\gamma_A (1+\alpha)} - 1,1 \cdot 10^7 r_h \omega_h \left(\frac{r_c}{I} \right)^{\frac{1}{5}} |sin\beta| \, tan\beta \sqrt{1 + tan^2\alpha \, cos^2\beta} \right\} \frac{\vec{R}}{R^2} \tag{67}$$

Herein $tan\beta$ is larger zero $\left(-\pi < \beta < -\frac{\pi}{2} \, ; \, \pi < \beta < \frac{3}{2}\pi \, ; \, 3\pi < \beta < \frac{7}{2}\pi, etc\right)$ for a right turn helix and negative $\left(-\frac{\pi}{2} < \beta < 0 \, ; \, \frac{3}{2}\pi < \beta < 2\pi; etc\right)$ for a left turn helix. By means of this vector expression the plasma behavior within the given MPD-thrusters (see Fig.( )) under onset conditions are discussed.

3.5 Plasmabehavior under Onset Conditions

As long as the expression $\left(\frac{I^{\frac{8}{5}}}{\dot{m}_c} r_c^{\frac{1}{5}}\right)$ stays well below $1,95 \cdot 10^9 \left[\frac{A^{\frac{8}{5}} m^{\frac{1}{5}}}{kg/s}\right]$, the $\omega_e \tau_e-$ effect on the conduction heat flux of the electrongas is still negligible for an argon MPD-flow. In this case the electrically conducting plasma is assumed to fill up the volume of the throat (on cylindrical part of the fluxed thruster) and the diverging part of the thruster nozzle. The discharge axis should therefore cioncide with the center line of the thruster and any deviation of the straight configuration should be meaningless since the discharge channel is "anchored" at the cathode tip and fixed by the chamber walls. If, however, $\left(\frac{I^{\frac{8}{5}}}{\dot{m}_c} r_c^{\frac{1}{5}}\right)$ comes close or even exceeds the critical value of $1,95 \cdot 10^9 \left[\frac{A^{\frac{8}{5}} m^{\frac{1}{5}}}{kg/s}\right]$ run away heating and a concentration of the discharge channel sets in. Simultaneously with the concentration one must expect an increase in the characteristics quantity $\left(\frac{I^{\frac{8}{5}}}{\dot{m}_c} r_c^{\frac{1}{5}}\right)$ since now a larger part of the gasflow streams outside of the hot more confined discharge channel yet; this part cannot be accounted any more to $\dot{m}_c$. As a consequence the quantity $\left(\frac{I^{\frac{8}{5}}}{\dot{m}_c} r_c^{\frac{1}{5}}\right)$ may increase even beyond a value of $1,7 \cdot 10^9 \sqrt{\gamma_A (1+\alpha)} \geq 2,3 \cdot 10^9 \left[\frac{A^{\frac{8}{5}} m^{\frac{1}{5}}}{kg/s}\right]$ what caused a dramatic change in the direction of the resultant transverse force, $\vec{\chi}_\perp$ which acts on the discharge channel per unit lenght [see eq.(67)]. Based on this proportionality formula, eq.(67), for $\vec{\chi}_\perp$ the following three cases have to be considered if run away heating, or onset is actived i.e. $\left(\frac{I^{\frac{8}{5}}}{\dot{m}_c} r_c^{\frac{1}{5}}\right) \geq 1,95 \cdot 10^9 \left[\frac{A^{\frac{8}{5}} m^{\frac{1}{5}}}{kg/s}\right]$.

$$\text{(a)} \qquad \left(\frac{I^{\frac{8}{5}}}{\dot{m}_c} r_c^{\frac{1}{5}}\right) < 1,7 \cdot 10^9 \sqrt{\gamma_A (1+\alpha)}$$

$$(b) \qquad \left(\frac{I^{\frac{8}{5}}}{\dot{m}_c} r_c^{\frac{1}{5}}\right) = 1,7 \cdot 10^9 \sqrt{\gamma_A (1+\alpha)} \tag{68}$$

$$\text{(c)} \qquad \left(\frac{I^{\frac{8}{5}}}{\dot{m}_c} r_c^{\frac{1}{5}}\right) < 1,7 \cdot 10^9 \sqrt{\gamma_A (1+\alpha)}$$

In case (a) the force $\vec{\chi}_\perp$ points into the negative $\vec{R}-$ direction. If an anchorde discharge channel experiences any small deviation $\left(\vec{\delta} \sim \vec{R}\right)$; see Fig.(27), the force $\vec{\chi}_\perp$ tends to straighten the column.

In this case, therefore, a straight discharge channel is stable. Within the diverging part of the nozzle the overheated constricted channel must be curved, however, in order to reach the anode ring. The radius of curvature becomes finite, and in order to fulfill the requirement, $\vec{\chi}_\perp = 0$, the brace expression of eq.(67) must be zero or the channel must be twisted i.e. assumes within the diverging part of the nozzle (see Fig.28).

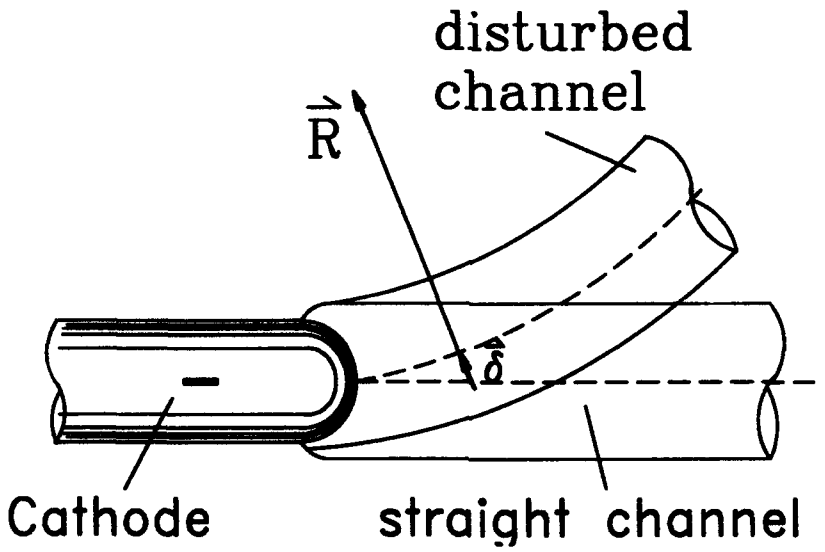

Figure 27: Illustration of a straight and disturbed anchored discharge channel

In thi· case for a right turn helix $(tan\alpha > 0)\omega_h$ must be negative or for a left turn helix $(tan\alpha < 0)\omega_h > 0$ in order to achive that the transverse force $\vec{\chi}_\perp$ becomes zero.

If, however, case (b) is reached, no twisted channel is necessary in order to obtain $\vec{\chi}_\perp = 0$ and ω_h can be zero. This means that the anode attachement sticks at a point and damages the anode locally by overheating which can indeed be observed when the preonset conditions are exceeded.

In case (c) the transverse force $\vec{\chi}_\perp$ per unit channel lenght (see eq.(67)) is zero if the channel is straight $(R \to \infty)$. Any small deviation $\left(\vec{\delta}\right)$ of the anchored arc channel (see Fig.27), however, now leads to an unstable channel behaviour or eventually to a curved and twisted channel. According to eq.(67) for a twist-free but disturbed (R finite) channel the brace expression is greater than zero, hence $\vec{\chi}_\perp$ acts in the direction of $\vec{R}\left(\sim \vec{\delta}\right)$ and tends to disturb the channel even further. Again a belanced configuration with $\vec{\chi}_\perp = 0$ can only be archived if the brace expression becomes zero, i.e. if the third term within the brace of eq.(67) becomes negative. In that case the discharge channel assumes a rotating helical shape whereby ω_h must be larger than zero for a right turn helix, and than zero for a left turn helix. It is interesting to note here that by increasing the quantity $\frac{I^{\frac{2}{5}} r_c^{\frac{1}{5}}}{\dot{m}_c}$ the helix should again straighten itself since now the brace expression becomes positive and therefore $\vec{\chi}_\perp$ acts in the direction of $\vec{R}$ and/or the brace expression becomes zero which means $tan\beta$ increases and therefore brings the discharge channel to a straighter configuration. Within the diverging part of the nozzle the helix continues in a conical fashion in order to end up on the anode ring. Since ω_h must be unequal zero, the helix and the anode attachment rotates again, now however, in the opposite direction than in case (a).

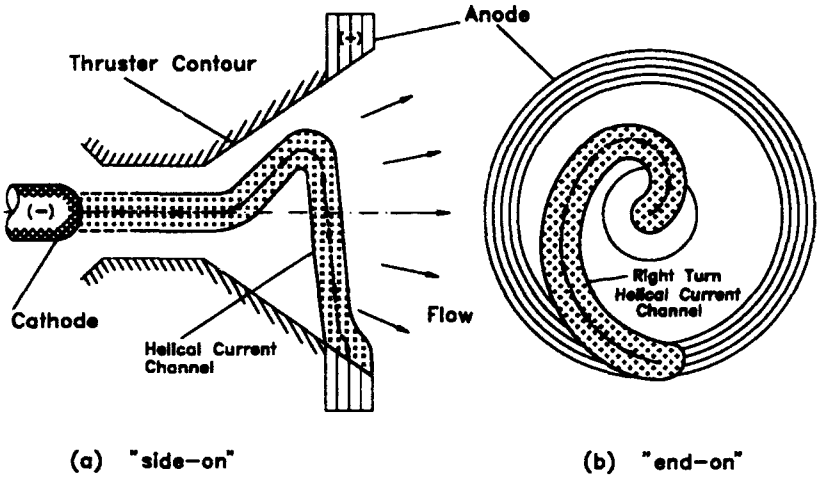

Figure 28: Helical discharge channel within nozzle

Summarizing it can be said that at 'onset' $\left(\frac{I^{\frac{2}{5}} r_c^{\frac{1}{5}}}{\dot{m}_c} \approx 2 \cdot 10^9 \left[\frac{A^{\frac{2}{5}} m^{\frac{1}{5}}}{kg/s}\right]\right)$ the discharge concentrates and assumes a helical shape within the diverging part of the nozzle. This conical helix rotates as long as the critical condition is not exceeded. If now the current is increased and/or the mass flow decreased beyond onset conditions, the rotation ceases and the anode attachment begins to stick, thereby damaging the anode irreversibly by local overheating. By further increasing the characteristic quantity $\frac{I^{\frac{2}{5}} r_c^{\frac{1}{5}}}{\dot{m}_c}$, the helix starts to turn again (now in the opposite direction than before). Since under these extreme conditions a straight discharge channel is unstable, plasma fluctuations near the cathode and within the constrictor should arise which may now damage the inner thruster walls.

4 List of Reports and Publications

During the period of the research grant the following reports and student thesis have been accomplished. Supported by this grant was either a part or the whole of each of the listed publications.

Papers

(Viareggio)	IEPC-91-087
	IEPC-91-022
(Nashville)	AIAA-92-3296

Thesis work

Kleinschmidt, J.:
Berechnung von MPD-Triebwerken unter Berücksichtigung eines variablen Ionisationsgrades. Studienarbeit, IRS Stuttgart, 1992.

Sleziona, P.C.:
Numerische Analyse der Strömungsvorgänge in magnetoplasmadynamischen Raumfahrtantrieben. Dissertation, IRS Stuttgart, 1992.

References

[1] Hügel, H:
On Compressible Plasma Flow in Self Magnetic Arc Thrusters (Zur Strömung kompressibler Plasmen im Eigenfeld von Lichtbogenentladungen), DLR-FB-70-13, 1970. Publishing Col: Wiss. Berichtswesen der DFVLR, Postfach 906058, D-5000 Köln 90.

[2] Sleziona, P.C., Auweter-Kurtz, M., Schrade, H.O., Wegmann, T.:
Comperison of Numerical and Experimental Investigations of MPD Accelerators. AIAA-90-2663, 21st International Electric Propulsion Conference, Orlando, FL, 1990.

[3] Auweter-Kurtz, M. and Messerschmid, E.W.:
Plasma Accelerator Activities at the University of Stuttgart. AIAA 90-2659; 21st International Electric Propulsion Conference, Orlando, Fl. 1990

[4] Auweter-Kurtz, M., Kurtz, H.L., Schrade, H.O., Sleziona P.C.:
Numerical Modeling of the Flow Discharge in MPD-Thrusters. Journal of Propulsion and Power, Vol. 5 No. 1, pp. 49–55, 1989.

[5] Schrade, H.O., Sleziona, P.C. and Kurtz, H.L.:
Basic Processes of Plasma Propulsion. Final Scientific Report, Grant AFOSR 86-0337, April 1991.

[6] Schrade, H.O., Wegmann, Th. and Rösgen, Th.:
The Onset Phenomena Explained by Run-Away Joule Heating. 22nd Intern. Electric Propulsion Conference, IEPC 91-022, Viaregggio, Italy, Oct. 1991.

[7] King, D.Q.:
Magnetoplasmadynamic Channel flow for Design of Coaxial MPD Thruster. Ph.D. Thesis, Department of Mechanical and Aerospace Engineering, Princeton University, 1981, also available as MAE Report 1552.

[8] Unsöld, A.:
Physik der Sternatmosphären. Springer, Berlin·Heidelberg·New York, 1968.

[9] Sleziona, P.C., Auweter-Kurtz, M., Schrade H.O.:
Numerical Evaluation of MPD Thrusters. IEPC 90-2602, 21st International Electric Propulsion Conference, Orlando, FL, 1990.

[10] Finkelnburg, W. und Maecker, H.:
Elektrische Bögen und thermisches Plasma. Handbuch der Physik Bd. XXII, Gasentladungen II, Springer, Berlin 1956.

[11] Schrade, H.O., Sleziona, P.C.:
Basic Processes of Plasma Propulsion. Interim Scientific Report, AFOSR Grant 86–0337, June 1990.

[12] Knoll, M. et. al.:
Gasentladungstabellen. Verlag von Julius Springer, Berlin, 1935.

[13] Maisenhälder, F., Mayerhofer, W:
Jet-diagnostics of a Self-Field Accelerator with Langmuir Probes, AIAA-Journal, Vol 12, No 9, Sept. 1974, pp. 1203-1209

[14] Sleziona,P.C., Auweter-Kurtz, M., Schrade, H.O., Wegmann, T.:
Comperison of Numerical and Experimental Investigations of MPD Accelerators. AIAA–90–2663, 21st International Electric Propulsion Conference, Orlando, FL, 1990.

[15] Eberle, A.:
Characteristic flux averaging approach to the solution of Euler's equations. VKI lecture series, Computational Fluid Dynamics, 1987–04, Brussels, Belgium, 1987.

[16] Burhorn, F.:
Berechnung und Messung der Wärmeleitfähigkeit von Stickstoff bis $13\,000° K$. Zeitschrift für Physik 155, Erlangen 1959.

[17] Hügel, H.:
Zur Funktionsweise der Anode im Eigenfeldbeschleuniger. DFVLR–FB 80–30, 1980

[18] Barnett, J.W. and Jahn, R.G.:
Operation of the MPD–Thruster with stepped Current Inputs. Dissertation for the Degree of Philosophy by J.W. Barnett, Mechan. and Aerospace Engeneering Princton Univ. April 1985 and J.W. Barnett and R.G. Jahn: Onset Phenomena in MPD–Thrusters. AIAA 85–2038, Oct. 1985

[19] Sovey, J.S. and Mantenieks, M.A.:
Performance and Lifetime Assessment of MPD–Arc Thruster Technology. NASA Tech. Memorandum 101293, AIAA–88–3211, 24th Joint Propulsion Conf., July 1988

[20] Kuriki, K. and Iida, H.:
Spectrum Analysis of Instabilities in MPD–Arcjet. IEPC 84–28, Proceedings of the 17th International Electric Propulsion Conference, Tokyo, 1984

[21] Baksht, F.G., Ya Moizhes, B. and Rybakov, A.B.:
Critical Regime of Plasma Accelerator Sov. Phys.. Tech. Phys. 18, p1613, 1974

[22] Shubin, A.P.:
Dynamic Nature of Critical Regimes in Steady State High–Current Plasma Accelerators. Sov. J. Plasma Phys. Vol. 2 p 18, 1976

[23] Cann, G.L. and Harder, R.L.:
Thrust Efficiencies of Electromagnetic Engines. AIAA 6 (3) p 558, 1966

[24] Uematsu, K. et al.:
Effect of Electrode Configuration on MPD–Arcjet Performance. 17th Int. Electric Propulsion Conf., IEPC 84–11, Tokyo 1984

[25] Wolff, M., Kelly, A.J. and Jahn, R.G.:
A High Performance Magnetoplsmadynamic Thruster. 17th Int. Electric Propulsion Conf., IEPC 84–32, Tokyo 1984

[26] Mallinaris, A.C. et al.:
Quasi–steady MPD Propulsion at High Power. Tech. Rep. AVSD–0146–71–RR, AVCO Corp. Wilmington Mass. (01887), NASA Rep. CR–0111872, 1971

[27] Korsun, A.G.:
Current Limiting by Self Magnetic Field in a Plasma Accelerator. Sov. Phys. Tech. Phys. 19 (1), July 1974

[28] Lawless, J.L. and Subramanian, V.L.:
A Theory of Onset in MPD- Thrusters. Scientific Report AFOSR 83–0033, 1983

[29] Schrade, H.O.:
Magnetoplasmadynamic Effects in Electric Arcs. Interim Scient. Report AFOSR 82–0298 Aug. 1983

[30] Schrade, H.O., Bez, W., Höcker, K.H. and Kaeppeler, H.J.:
Zur Theorie der ohm'schen Heizung vollionisierter Plasmen. Z.f. Naturforschung, Vol.15a, p.155, 1960

[31] Chapman, S.and Cowling, T.G.:
The Mathematical Theory of Non Uniform Gases. Cambridge University Press Third Edition p.868 f 1970

[32] Schrade, H.O., Auweter-Kurtz, M., Kurtz, H.L.:
Stability Problems in Magnetoplasmadynamic Arc Thrusters. 18th Fluid Dynamics and Plasmadynamics and Laser Conf. AIAA 85–1633, Cincinatti, Ohio, July 1985